On the analysis of heat haze effects with spacetime DIC

Myriam Berny, Thibaut Archer, Anne Mavel, Pierre Beauchêne, Stéphane Roux, François Hild

On the analysis of heat haze effects with spacetime DIC

Myriam Berny[a,b], Thibaut Archer[a,c,b], Anne Mavel[c], Pierre Beauchêne[c], Stéphane Roux[a], François Hild[a,*]

[a] *LMT (ENS Paris-Saclay / CNRS / University Paris-Saclay)*
61 avenue du Président Wilson, 94235 Cachan (France)
[b] *SAFRAN, Safran Ceramics, Le Haillan, France*
[c] *ONERA, The French Aerospace Lab*
29 avenue de la Division Leclerc, 92320 Châtillon, France

Abstract

Long image series (*i.e.,* movies) can be analyzed via digital image correlation (DIC) techniques. A new spacetime implementation is introduced to extend instantaneous DIC with minimal implementation complexity. With this procedure, a denoised reference image is built considering a series of more than 200 images. Such spacetime approach is very interesting when high temperature experiments are performed since it provides a very effective temporal regularization. The analysis of heat haze effects is carried out on a thermomechanical test in which the sample made of ceramic matrix composite is subjected to temperatures greater than 1,200°C in the heat affected zone of the laser beam. It is shown that the addition of a small fan reduces the spurious displacement fluctuations.

Keywords: Denoising, Global DIC, Heat haze, High temperature test, Spatiotemporal regularization

*Corresponding author. Email: francois.hild@ens-paris-saclay.fr

1. Introduction

High temperature applications (*e.g.,* for aircraft engines) require the development of new materials in order to meet stringent regulations in terms of NO_x emissions [1]. Ceramic matrix composites are one route that is currently investigated [2, 3], some of them barrier coated [4]. To determine their thermomechanical properties, high temperature tests need to be performed [5, 6, 7, 8, 9]. Their quantitative monitoring can be achieved with non-contact techniques. Among the latter ones [10], Digital Image Correlation (DIC) is one possible option [11].

DIC was utilized to analyze high temperature experiments since the pioneering work of Lyons et al. [12]. The authors showed its feasibility for temperatures up to 650°C for specimen subjected to rigid body translations, thermal expansion and tensile loads. Experiments were then conducted on nickel-based super-alloy up to 700°C in order to investigate creep crack growth [13]. Reliable DIC measurements were subsequently reported up to 1,200°C [14, 15, 16]. Novak and Zok [17] reached temperatures as high as 1,500°C with careful control of the illumination and filtering, and minimization of heat haze effects.

Pan et al. [18] showed that ordinary equipment can be used to evaluate coefficients of thermal expansion of various metallic materials for maximum temperatures of 600°C. Leplay et al. [19] studied the damage behavior of aluminum titanate by performing four-point flexural tests up to 900°C. Later on, the asymmetric creep behavior of an industrial zircon ceramic was reported [20] for a temperature of 1,350°C. Virtually all the above-cited works only used one camera (*i.e.,* for so-called 2D DIC [21]). Stereocorrelation was

also shown to be applicable in high temperature experiments [17]. The coefficient of thermal expansion of stainless steels was evaluated during a cooling phase starting at 600°C outside the furnace used to heat up the samples [22].

From this literature review, three important points to address arise:

1. Because of so-called black body radiations, brightness conservation, which is the underlying principle of DIC, is no longer satisfied [12]. Various solutions have been proposed for local [11] and global [23, 24] approaches. The use of powerful lighting devices is one possible answer up to temperatures of the order of 800°C. Another route is to utilize band pass filters to reach higher temperatures [14, 18, 15, 20] or use ultra-violet light [25].
2. Another critical issue is linked to image contrast, which is necessary for DIC analyses [11, 26]. It was shown that regular black and white paints were sufficient up to 300°C [27], and so-called high temperature paints could be used up to 600°C. This is no longer possible at higher temperatures [22, 16]. For instance, Lyons et al. [12] showed that boron nitride combined with aluminum oxide could be used. Pan et al. [15] utilized cobalt oxide mixed with inorganic adhesive in order to reach temperatures up to 1,200°C.
3. In high temperature experiments thermal gradients unavoidably occur between the (hot) sample and the (general cold) camera lens. These gradients induce variation of the refractive index, except when the test is performed in vacuum. These temperature gradients induce artifacts for the optical path. Time varying thermal gradients, say in the air, are due to convection at high temperatures. This phenomenon leads

to the so-called heat haze effect, which can be limited by using forced air flux [12, 16, 17]. Heat haze effects are strongly dependent on the experimental configuration. The worst case is believed to occur in traditional furnaces since a large amount of air is concerned [12, 19, 16, 20]. Other heating means can be selected such as heat induction [14], laser [17] or infrared [18, 15] sources.

In the following, it is proposed to investigate heat haze effects at high temperatures, when the sample is heated with a laser source, via spatiotemporal DIC analyses. As for spatial registrations, for which local and global analyses are possible [28], temporal analyses can either be instantaneous (*i.e.,* two pictures are correlated for each time step [11]), or local time interpolations can be used to evaluate strain rate fields [29], or global temporal interpolations over the whole time domain [30, 31]. The time basis functions can be either very generic [31], based upon a priori analyses [32, 33] or constructed during the registration procedure [34]. Generic temporal shape functions will be considered in which a new spacetime implementation will be proposed and investigated.

2. Spatiotemporal Digital Image Correlation

2.1. Spatiotemporal framework

Global spacetime registrations consist in measuring the displacement field $\boldsymbol{u}(\boldsymbol{x},t)$ for a series of images $f(\boldsymbol{x},t)$ that minimize the overall gap to gray level conservation [31]

$$\boldsymbol{u}(\boldsymbol{x},t) = \text{argmin}_{\boldsymbol{v}} \|f(\boldsymbol{x}+\boldsymbol{v}(\boldsymbol{x},t),t) - f(\boldsymbol{x},t_0)\|^2_{\text{ROI}\times[t_0,t_1]} \tag{1}$$

where $\boldsymbol{x}$ denotes any pixel location within the spatial region of interest (ROI), $t \in [t_0, t_1]$ the time at which the picture was acquired, and $\| \bullet \|$ the Euclidian norm. In the present formulation, the reference picture corresponds to the first acquired image $f(\boldsymbol{x}, t_0)$. The latter, which is corrupted by noise as any of the subsequent pictures, appears in all the registrations be they instantaneous or global in time and induces a "persistent" fluctuation in the measured displacements [31]. The way to mend this problem is to add a new unknown to the registration problem, which is the reference image *itself* $\widehat{f}(\boldsymbol{x})$ so that spacetime registration now becomes

$$\boldsymbol{u}(\boldsymbol{x}, t) = \text{argmin}_{\boldsymbol{v}} \| f(\boldsymbol{x} + \boldsymbol{v}(\boldsymbol{x}, t), t) - \widehat{f}(\boldsymbol{x}) \|^2_{\text{ROI} \times [t_0, t_1]} \tag{2}$$

provided $\widehat{f}$ (or an estimate thereof) is known. This point will be discussed in Section 2.3. In the following discussion, it is thus assumed that $\widehat{f}$ is known (*e.g.*, $\widehat{f}(\boldsymbol{x}) = f(\boldsymbol{x}, t_0)$ as an initial guess). In spirit, this writing is close to that proposed for multiview correlations [35]. The difference here is that the image sequence acquired with a single camera is utilized in order to estimate the reference configuration instead of using multiple cameras for a single time step. Both approaches may be combined to perform spacetime registrations using images shot by multiple cameras.

Given the fact that spacetime analyses are to be run, the sought displacement field is parameterized as

$$\boldsymbol{u}(\boldsymbol{x}, t) = \sum_{i=1}^{n_x} \sum_{j=1}^{n_t} a_{ij} \boldsymbol{\theta}_i(\boldsymbol{x}) \phi_j(t) \tag{3}$$

where a space/time separation is assumed in which $\boldsymbol{\theta}_i$ denote the spatial shape functions (associated with n_x degrees of freedom), and ϕ_j the temporal shape functions (with n_t degrees of freedom). The determination of

the $n_x \times n_t$ unknown amplitudes a_{ij} is performed, for instance, by using Gauss-Newton's scheme [31] in order to minimize the overall gap to gray level conservation (2). The amplitude corrections, which are gathered in the column vector $\{\delta \boldsymbol{a}\}$, are iteratively updated by solving linear systems

$$[\boldsymbol{H}]\{\delta \boldsymbol{a}\} = \{\boldsymbol{B}\} \tag{4}$$

where $[\boldsymbol{H}]$ is the spatiotemporal Hessian, and $\{\boldsymbol{B}\}$ the spatiotemporal right hand side vector.

2.2. Modal decomposition

In the following, a special setting is considered. It allows regular (*i.e.,* instantaneous) DIC codes to be extended to spacetime analyses with minimal changes. In particular, when kernels are available [36] to compute the spatial Hessian $[\boldsymbol{M}]$ and instantaneous right hand side vector $\{\boldsymbol{b}(t)\}$ dependent on the pixel-wise gray level residuals, they will be used in the proposed implementation as well since there will be no need for assembling the global spatiotemporal Hessian $[\boldsymbol{H}]$.

The spatiotemporal Hessian $[\boldsymbol{H}]$ can be decomposed in the following way thanks to the space/time separation of the sought displacement field [31]

$$H_{ijkl} = M_{ik}\Phi_{jl} \tag{5}$$

with

$$\Phi_{jl} = \sum_{t_0}^{t_1} \phi_j(t)\phi_l(t) \tag{6}$$

If the temporal shape functions are orthogonal and normalized (*i.e.,* $\Phi_{jl} = \Delta_{jl}$, where $[\boldsymbol{\Delta}]$ is Kronecker delta matrix), each iteration consists in independently solving n_t linear systems with the spatial Hessian $[\boldsymbol{M}]$, namely,

similar to any instantaneous computation. The main difference is related to the construction of the residual vector that accounts for the fact that the temporal shape functions may span over the whole time interval $[t_0, t_1]$.

Depending on the choice of the temporal shape functions $\phi_j(t)$, the previous property is not necessarily satisfied. In that case, the global operator $[\boldsymbol{\Phi}]$ may be diagonalized

$$[\boldsymbol{\Phi}] = [\boldsymbol{V}][\boldsymbol{D}][\boldsymbol{V}]^\top \tag{7}$$

where $[\boldsymbol{V}]$ denotes the (orthogonal) matrix whose columns are the right eigen vector components, and $[\boldsymbol{D}]$ the diagonal matrix containing the corresponding eigen values.

If the temporal modes $[\boldsymbol{\psi}]$ are *defined* as

$$[\boldsymbol{\psi}] = [\boldsymbol{D}]^{-1/2}[\boldsymbol{V}]^\top[\boldsymbol{\phi}] \tag{8}$$

where each line k of $[\boldsymbol{\psi}]$ corresponds to a temporal mode $\psi^k(t)$ or equivalently

$$[\boldsymbol{\phi}] = [\boldsymbol{V}][\boldsymbol{D}]^{1/2}[\boldsymbol{\psi}] \tag{9}$$

then

$$[\boldsymbol{\Psi}] \equiv [\boldsymbol{\psi}][\boldsymbol{\psi}]^\top = [\boldsymbol{\Delta}] \tag{10}$$

by construction. Consequently, for each mode ψ^k, the linear system to solve becomes

$$[\boldsymbol{M}]\{\delta\boldsymbol{\alpha}^k\} = \{\boldsymbol{\beta}^k\} \tag{11}$$

with

$$\{\boldsymbol{\beta}^k\} = \sum_t \{\boldsymbol{b}(t)\}\psi^k(t) \tag{12}$$

where $\{\delta\boldsymbol{\alpha}^k\}$ are the corrections to the spatial degrees of freedom associated with the k-th mode. By looping over the n_t modes, all the $n_x \times n_t$ corrections

are obtained. Let us emphasize that the spacetime analysis has been turned into n_t *uncoupled* DIC problems where the computation load is similar to instantaneous DIC.

The last step is to update the gray level residuals

$$\rho(\boldsymbol{x},t) = \widehat{f}(\boldsymbol{x}) - f(\boldsymbol{x}+\boldsymbol{u}_m(\boldsymbol{x},t),t) \tag{13}$$

in order to evaluate all instantaneous right hand side vectors $\{\boldsymbol{b}(t)\}$ for the current estimate $\boldsymbol{u}_m$ of the displacement field. Let matrix $[\boldsymbol{U}]$ gather the nodal displacement vectors for all acquired pictures (*i.e.,* it is of dimension $n_x \times n_f$)

$$[\boldsymbol{U}] = [\boldsymbol{\alpha}][\boldsymbol{\psi}] \tag{14}$$

Each column $\{\boldsymbol{U}(t)\}$ is used to compute the current estimate of the displacement field once the values of each spatial shape functions are computed for each pixel location $\boldsymbol{x}$ of the ROI

$$\boldsymbol{u}_m(\boldsymbol{x},t) = [\boldsymbol{\Theta}(\boldsymbol{x})]\{\boldsymbol{U}(t)\} \tag{15}$$

This displacement field is utilized to compute the pictures in the deformed configurations $f(\boldsymbol{x},t)$ corrected by the measured displacement field $\boldsymbol{u}_m$

$$\widetilde{f}_{\boldsymbol{u}}(\boldsymbol{x},t) = f(\boldsymbol{x}+\boldsymbol{u}_m(\boldsymbol{x},t),t) \tag{16}$$

The implementation of global spacetime DIC is detailed in Algorithm 1. The inputs are all the acquired pictures $f(\boldsymbol{x},t)$, the reference image $\widehat{f}(\boldsymbol{x})$ from which the spatial Hessian matrix $[\boldsymbol{M}]$ is constructed. The node to pixel transformation matrix $[\boldsymbol{\Theta}(\boldsymbol{x})]$ is computed once for all since it is associated with spatial shape functions. Similarly, all the matrices associated with the

temporal shape functions (*i.e.,* $[\boldsymbol{\phi}], [\boldsymbol{\Psi}], [\boldsymbol{V}], [\boldsymbol{D}]$) are pre-computed. Last, initial guesses to the sought degrees of freedom may be given (otherwise, they are assumed to be zero). They are gathered in the $n_x \times n_t$ matrix $[\boldsymbol{a}_0]$. With the chosen modal decomposition, the corresponding initial guess reads

$$[\boldsymbol{\alpha}_0] = [\boldsymbol{a}_0][\boldsymbol{V}][\boldsymbol{D}]^{1/2} \tag{17}$$

The iterative scheme then starts. The first step is to compute the gray level residuals $\rho(\boldsymbol{x}, t)$ for all pictures, then the instantaneous residual vectors $\{\boldsymbol{b}(t)\}$ are evaluated, and from them the modal right hand side vectors $\{\boldsymbol{\beta}^k\}$. A loop over all the n_t modes is performed to assess all new corrections $[\delta\boldsymbol{\alpha}]$ in order to update $[\boldsymbol{\alpha}]$. Since the convergence criterion is written in terms of the norm of the correction matrix $[\delta\boldsymbol{a}]$, the latter is computed from matrix $[\delta\boldsymbol{\alpha}]$. In the following, a value of $\epsilon_a = 10^{-6}$ pixel is chosen, which is very severe. An escape condition allows the interruption of the iterative scheme when a maximum number of iterations is reached.

Algorithm 1 Spacetime-DIC algorithm

procedure SPACETIME-DIC

while $\|\boldsymbol{\delta a}\| > \epsilon_a$ **do**

$[\boldsymbol{U}] \leftarrow [\boldsymbol{\alpha}][\boldsymbol{\psi}]$, $\boldsymbol{u}(\boldsymbol{x},t) = [\boldsymbol{\theta}(\boldsymbol{x})]\{\boldsymbol{U}(t)\}$ ▷ Spacetime disp.

$\rho(\boldsymbol{x},t) \leftarrow \widehat{f}(\boldsymbol{x}) - \widetilde{f}_{\boldsymbol{u}}(\boldsymbol{x},t)$ ▷ Residuals

$b_i(t) \leftarrow \sum_{\boldsymbol{x}} \rho(\boldsymbol{x},t)(\boldsymbol{\theta}_i(\boldsymbol{x}) \cdot \boldsymbol{\nabla}\widehat{f}(\boldsymbol{x}))$ ▷ Right hand side vectors

for $k \leftarrow 1, n_t$ **do**

$\{\boldsymbol{\alpha}^k\} \leftarrow k$-th column of $[\boldsymbol{\alpha}]$

$\beta_i^k \leftarrow \sum_t b_i(t)\psi_k(t)$ ▷ Modal residual vector

$\{\delta\boldsymbol{\alpha}^{\boldsymbol{k}}\} \leftarrow [\mathbf{M}]^{-1}\{\boldsymbol{\beta}^k\}$ ▷ Resolution per mode

$\{\boldsymbol{\alpha}^{\boldsymbol{k}}\} \leftarrow \{\boldsymbol{\alpha}^{\boldsymbol{k}}\} + \{\delta\boldsymbol{\alpha}^{\boldsymbol{k}}\}$ ▷ Update of modal disp. vector

end for

$[\delta\boldsymbol{a}] \leftarrow [\delta\boldsymbol{\alpha}][\boldsymbol{D}]^{-1/2}[\boldsymbol{V}]^\top$

end while

$[\boldsymbol{U}] \leftarrow [\boldsymbol{\alpha}][\boldsymbol{\psi}]$, $\boldsymbol{u}(\boldsymbol{x},t) = [\boldsymbol{\theta}(\boldsymbol{x})]\{\boldsymbol{U}(t)\}$ ▷ Converged spacetime disp.

$\rho_{conv}(\boldsymbol{x},t) \leftarrow \widehat{f}(\boldsymbol{x}) - \widetilde{f}_{\boldsymbol{u}}(\boldsymbol{x},t)$ ▷ Residuals at convergence

return $\boldsymbol{u}, \rho_{conv}$ ▷ Displacement and residuals

end procedure

2.3. Construction of a denoised reference image

The previous step was based upon the knowledge of the so-called denoised reference image $\widehat{f}$. Algorithm 2 shows how this a priori unknown picture is computed. All the precomputation steps mentioned above have to be performed. Further, an initial guess for $\widehat{f}$ is required. Various routes can be followed depending on the situation. The most natural choice consists in choosing the first acquired picture $f(\boldsymbol{x}, t_0)$ as an initial estimate. If it

were not updated, it would basically correspond to the spacetime framework introduced in Ref. [31]. If more than one picture of the reference configuration are acquired (this is often the case in order to assess the noise level and measurement resolutions [28]), then the average of all these pictures is a better choice (as the noise level could already be reduced by averaging). Another choice may be associated with the fact that instantaneous calculations were run prior to the spacetime analysis so that an initial guess for the sought amplitudes a_{ij} may be inferred [31]. In such cases, all the corrected images $\widetilde{f}_{\boldsymbol{u}}(\boldsymbol{x},t)$ are estimates of the reference image. Their temporal average $\langle\widetilde{f}_{\boldsymbol{u}}(\boldsymbol{x},t)\rangle_t$ is a good first guess.

The proposed implementation is based on the previous observation. Until the root mean square difference of two consecutive estimates of $\widehat{f}$ becomes lower than a chosen threshold ϵ_f (here taken equal to 10^{-2} gray level, see Section 3.3), spacetime DIC analyses (Algorithm 1) are run. Once (inner) convergence is obtained, new estimates of $\widetilde{f}_{\boldsymbol{u}}(\boldsymbol{x},t)$ are available. In order to preserve the details in the reference image, $\widehat{f}$ is not replaced by the time average of all the corrected images. An under-relaxation is performed with parameter $0 \leq \omega \leq 1$

$$\widehat{f}(\boldsymbol{x}) = (1-\omega)\widehat{f}_{old}(\boldsymbol{x}) + \omega\langle\widetilde{f}_{\boldsymbol{u}}(\boldsymbol{x},t)\rangle_t \tag{18}$$

Otherwise, an imperfect initial estimate of the sought displacement field may produce blurred images $\langle\widetilde{f}_{\boldsymbol{u}}(\boldsymbol{x},t)\rangle_t$ that may hamper or slow down (global) convergence. A value of $\omega = 0.5$ will be used in the sequel.

Algorithm 2 Complete spacetime-DIC algorithm

procedure COMPLETE SPACETIME-DIC
  $[\boldsymbol{\phi}]$, $[\boldsymbol{\Psi}]$, $[\boldsymbol{V}]$, $[\boldsymbol{D}]$ ▷ Temporal shape functions and diagonalization
  $[\boldsymbol{a}_0]$, $[\boldsymbol{\alpha}_0]$ ▷ Initialization of spacetime DOFs
  $\widehat{f}(\boldsymbol{x}) \leftarrow \widehat{f}_0(\boldsymbol{x})$ ▷ Initialization of reference image
  while $\|\widehat{f}(\boldsymbol{x}) - \widehat{f}_{old}(\boldsymbol{x})\| > \epsilon_f$ **do**
    $\Theta_i(\boldsymbol{x}) \leftarrow \boldsymbol{\theta}_i(\boldsymbol{x}) \cdot \boldsymbol{\nabla}\widehat{f}(\boldsymbol{x})$
    $M_{ij} \leftarrow \sum_{\boldsymbol{x}} \Theta_i(\boldsymbol{x})\Theta_j(\boldsymbol{x})$ ▷ Spatial DIC matrix
    call procedure SPACETIME-DIC
    $\widehat{f}_{old}(\boldsymbol{x}) \leftarrow \widehat{f}(\boldsymbol{x})$
    $\widehat{f}(\boldsymbol{x}) \leftarrow \widehat{f}(\boldsymbol{x}) - \dfrac{\omega}{n_t}\sum_t \rho_{conv}(\boldsymbol{x}, t)$ ▷ Update reference image
  end while
  return $\widehat{f}, \boldsymbol{u}, \rho_{conv}$
end procedure

For all the results discussed hereafter, the spatial parameterization of the measured displacement fields will be based on finite element discretizations with 3-noded triangles (*i.e.,* T3-DIC [37]). The temporal discretizations will be affine for each considered time increment, which is greater than one image (*i.e.,* at least 20 pictures will be considered in each increment). The implementation is performed within the Correli 3.0 framework, which is a Matlab code where the time consuming operations (*e.g.,* computation of gray level residuals) are performed in C++ kernels called as MEX files [36].

3. SiC/SiC Composite heated at very high temperatures

3.1. Experimental setup

A sample made of SiC/SiC composite was heated at very high temperatures thanks to a CO_2 laser beam [38]. Under such thermal gradients, the material expands and deflects. To measure the thermomechanical fields of the sample, a set of four cameras was installed (Figure 1). Three cameras monitored the top surface of the studied CMC, which was heated by the laser beam, in order to measure temperature fields during the test (with an infrared camera FLIR X6580sc®, acquiring frames at a frequency of 1 Hz) and 3D surface displacement fields (*i.e.,* stereovision system composed of two AVT Pike-421® cameras with 2.8/50 lenses). (Dark) SiC power was deposited since the composite surface was naturally white matte. The temperature of the back face of the sample was measured thanks to two pyrometers monitoring points in the hottest area, namely, one bi-chromatic pyrometer (IGAR 6 Advanced of LumaSense®, temperature range: 200-2000°C, spectral band: 1.5-1.6 µm) and one monochromatic pyrometer (MI3 made by Raytek®, temperature range: -40 to 1650°C, spectral band: 8-14 µm). An additional optical camera (AVT Pike-421® with 4/80 lens and 41 mm extension ring) was positioned to observe the edge of the CMC beam. LED lights (7700 lm) were installed. In the following, only the pictures acquired by the last camera will be analyzed. The pictures acquired by the infrared camera and the stereovision system will not be analyzed herein. To measure 2D displacements, the edge of the sample is first coated with a homogeneous layer of white paint then speckled with black paint. The correlation radius of the speckle pattern is equal to 3 pixels, which indicates an overall good

quality. Both paints (OMAT® 7/75; MSRR 9176 produced by Indestructible Paint) are resistant to very high thermal shocks (*i.e.*, up to 1,000°C).

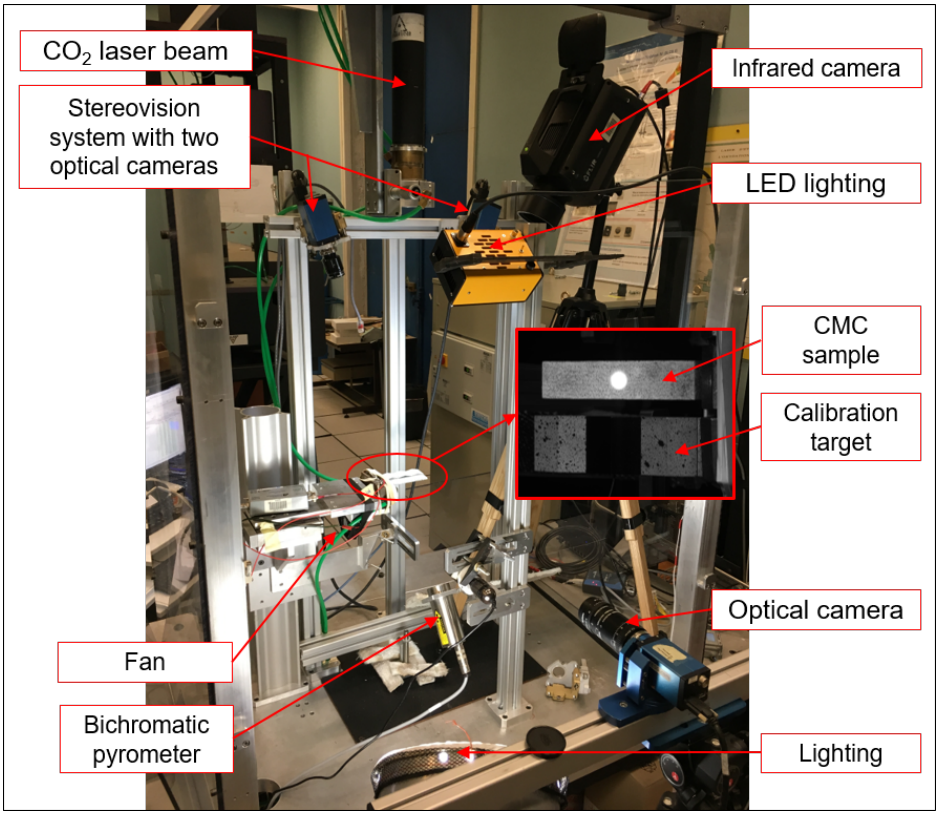

Figure 1: Multi-camera setup of a SiC/SiC composite heated at very high temperatures by a laser beam.

Three steps were performed with the present setup (Figure 2):

1. A series of controlled horizontal displacements was carried out thanks to a micrometer screw at room temperature for the purpose of calibrating the stereovision system. In the present case, the calibration target (see inset of Figure 1) was not removed before turning on the laser source.

For each level of the calibration phase, about 20 images were acquired at a frequency of 1.25 Hz. The first level corresponded to a reference state with no motion, the eight following levels were performed for translation increments of 0.5 mm, and the last state consisted in a return to the 0 mm position with no backlash compensation. A total of 217 pictures was captured.

2. Heating/cooling performed with the laser beam with no fan to homogenize the atmosphere around the heat affected zone. Three levels of temperature were analyzed: $0.4T_{\max}$, $0.7T_{\max}$ and $T_{\max}$, where $T_{\max}$ was greater than 1,200°C and corresponded to the maximum temperature of the heat affected zone by the laser beam (see inset of Figure 1). In the following, dimensionless levels $T/T_{\max}$ will be reported. The times corresponding to the beginning and end of transient/steady increments are shown in Figure 2. Overall, 3,218 images were acquired at a frequency of 1.25 Hz.
3. A final heating phase was performed with a fan (Figure 1). The same levels of steady state temperatures were reached (Figure 2). In total 2,485 pictures were acquired at a frequency of 1.25 Hz.

During the experiment, the laser power was regulated, leading to very small temporal fluctuations of the three steady-state levels (*e.g.,* at $T_{\max}$ when the fan was turned off (resp., turned on), the standard fluctuations were equal to 10°C (resp., 3°C)).

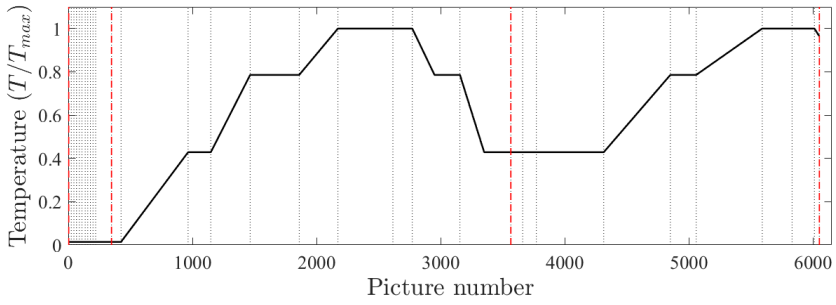

Figure 2: Three different test steps. The black solid line corresponds to the dimensionless temperature, the vertical dotted lines depict time increments and the vertical red dashed lines indicate the three test steps.

Figure 3 shows one picture acquired during the first, second and third steady state temperature levels of the second step (*i.e.,* heating with fan off). Because of black body radiations, the gray levels saturate in an area close to the heat affected zone. In that area, instantaneous DIC cannot converge since gray level conservation is violated and image contrast vanishes. It does converge when spatially regularized approaches are used in which regularization compensates for missing DIC information.

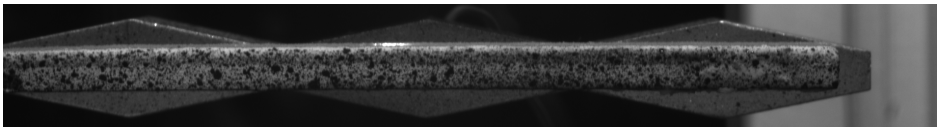

(a) $T = 0.4T_{\max}$

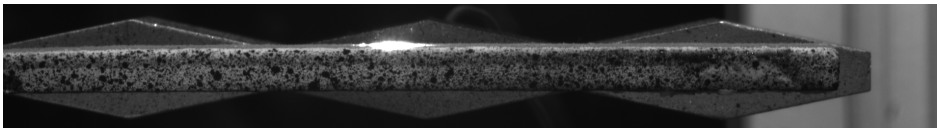

(b) $T = 0.7T_{\max}$

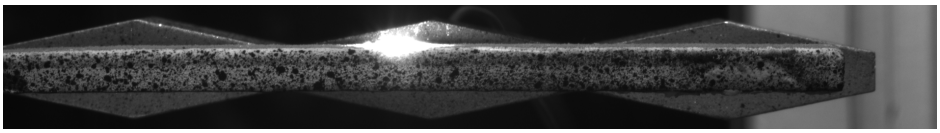

(c) $T = T_{\max}$

Figure 3: Pictures of the sample surface taken during the first (a), second (b), and third (c) temperature levels (heating with no fan).

3.2. Calibration step

The calibration step is used to construct a denoised reference image via spacetime DIC. The displacement uncertainties are also estimated.

3.2.1. Instantaneous approach

First, instantaneous DIC is run on the images for each calibration step for a region of interest (ROI) of definition 1385×60 pixels, which is meshed with 88 3-noded triangles (T3), as shown in Figure 4. The element size ranges from approximatively 30 pixels to 75 pixels for the center area, which corresponds to the zone saturated by laser heating during the second and third levels (see Figure 3). The first reference image, which is shown in

Figure 4, is constructed as the mean of the 21 images taken for the reference configuration (*i.e.*, initial 0 mm position).

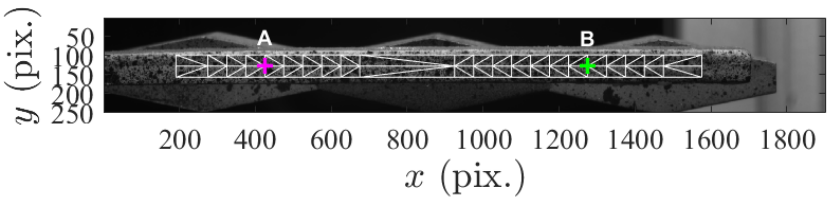

Figure 4: Initial reference image $\widehat{f}_0(\boldsymbol{x})$ with the meshed region of interest. The two crosses indicate the positions of the nodes whose displacements are highlighted in Figure 5.

For the calibration step, global DIC is performed between the estimated reference image and all acquired images. The instantaneous spatial displacement $\boldsymbol{u}(\boldsymbol{x}, t)$ is initialized with zero values if it is the first level with no applied displacement ($\boldsymbol{u}(\boldsymbol{x}, t = t_0) = \boldsymbol{0}$), or by the sum of the converged displacement for the previous time $\boldsymbol{u}(\boldsymbol{x}, t-1)$ and the mean translation $\boldsymbol{u}_{FFT}(t)$ estimated by Fast Fourier Transform correlation between the previous image $f(\boldsymbol{x}, t-1)$ and the current image $f(\boldsymbol{x}, t)$. Convergence is probed with the norm of the correction vector of nodal displacements. A value $\epsilon_a = 10^{-4}$ pixel is chosen.

The horizontal and vertical displacements (respectively, $u_x(t)$ and $u_y(t)$) are reported in Figure 5 for all the nodes, and the two nodes (depicted in Figure 4) with the lowest and highest variations are highlighted in Figure 5(b). The results are consistent with the experimental procedure, that is incremental (0.5 mm) horizontal displacements corresponding to approximately 10.5 pixels. The vertical displacement drift can be explained by a misalignment of the sample of about 0.5° with respect to the direction of applied

displacement.

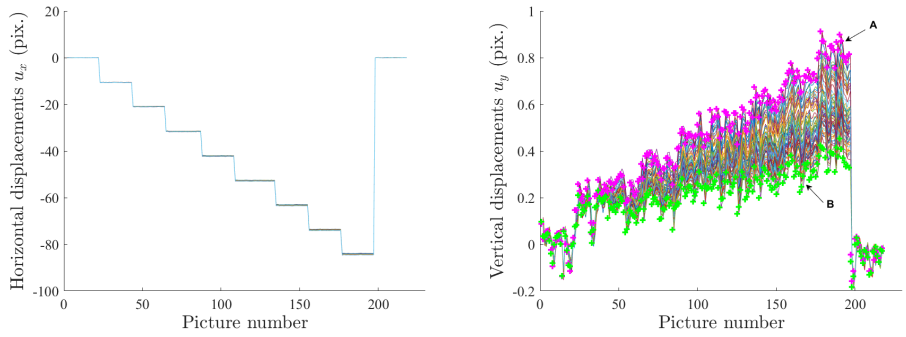

(a) (b)

Figure 5: Horizontal $u_x(t)$ (a), and vertical $u_y(t)$ (b) nodal displacements (expressed in pixels) measured with instantaneous DIC of images of the calibration phase. The magenta (roughly the highest u_y over the entire image series) and green (roughly the lowest u_y over the entire image series) crosses correspond to nodes A and B respectively depicted in Figure 4.

For each nodal displacement, the standard deviation for the considered time increment characterizes the standard uncertainty. Its average level for all nodes is reported in Figure 6 for all time increments. The uncertainties on horizontal and vertical displacements (resp., u_x and u_y) are similar during the whole calibration phase, with levels of the order of 0.04 pixel for any prescribed displacement level. This uncertainty level is due to camera noise and possible variations of lighting intensity and reflections induced by sample motions.

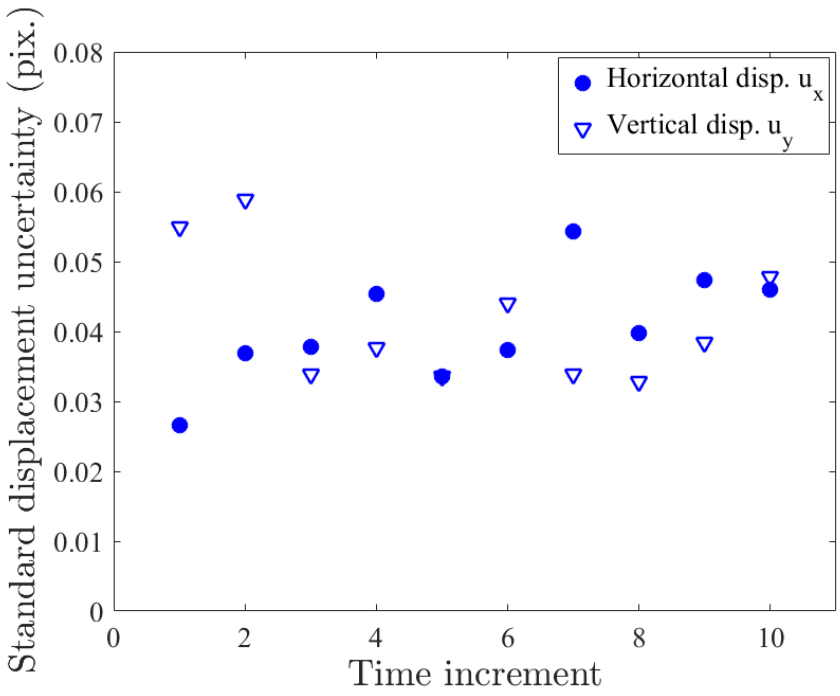

Figure 6: Standard displacement uncertainty for each time increment of the calibration step.

3.3. Construction of denoised reference image

In the sequel, the calibration step of the experiment is further analyzed in order to construct a denoised reference image $\widehat{f}(\boldsymbol{x})$ via spacetime DIC. The reference image $\widehat{f}_0(\boldsymbol{x})$ is initialized with the previously introduced reference image (Figure 4). An affine basis of temporal shape functions is considered (Figure 7(a)) with discontinuities between each time increment. For the first increment (*i.e.,* reference state), only one linear function is selected so that the displacement for the first image $\boldsymbol{u}(\boldsymbol{x}, t = t_0)$ is forced to $\mathbf{0}$.

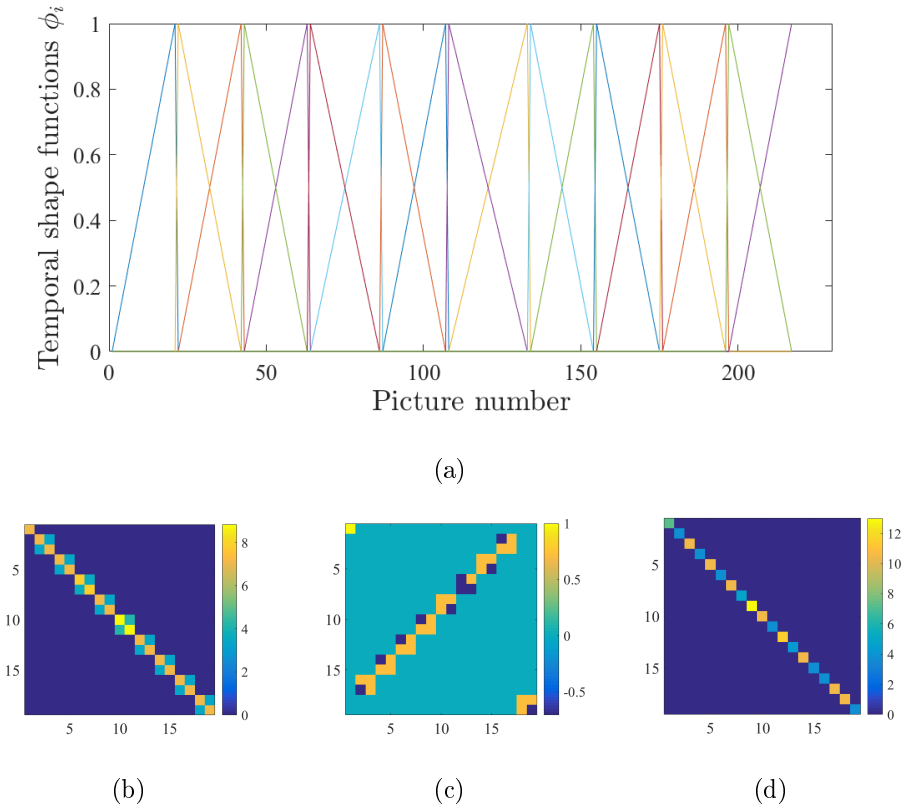

Figure 7: Temporal shape functions evaluated for each frame of the calibration step. Corresponding (b) Global temporal operator [$\boldsymbol{\Phi}$], (c) eigenvector matrix [$\boldsymbol{V}$], and (d) diagonal matrix [$\boldsymbol{D}$].

The associated global temporal operator [$\boldsymbol{\Phi}$], diagonal matrix [$\boldsymbol{D}$] and eigenvector matrix [$\boldsymbol{V}$] are shown in Figure 7. Because the temporal shape functions are discontinuous, independent blocks are obtained in the global temporal operator [$\boldsymbol{\Phi}$] (Figure 7(b)). Consequently, the eigenvector matrix is also block-diagonal with $\pm\sqrt{2}/2$ values, except the first block, which involves only one shape function (Figure 7(c)). In the present case, the eigen values

range from 3.85 and 13 (see Figure 7(d)), which shows that the conditioning of the global temporal operator $[\boldsymbol{\Phi}]$ is very good.

The spatiotemporal displacements $[\boldsymbol{a}_0]$ are initialized by performing instantaneous DIC analyses using Fast Fourier Transforms (to evaluate rigid body translations) between the reference image and any picture of the considered time increments. At the end of the complete spacetime algorithm, which converged in approximatively 18 min on a standard laptop computer (16 Go RAM, core i7 processor running at 2.7 GHz), the root mean square gray level residual has dropped from 1.83 (*i.e.*, 0.74 % of the dynamic range of $\widehat{f}_0$) to 1.32 (*i.e.*, 0.53 % of the dynamic range of $\widehat{f}$), and the norm of the difference between two successive reference images $\|\widehat{f}(\boldsymbol{x}) - \widehat{f}_{old}(\boldsymbol{x})\|$ stabilizes at 1.3×10^{-3} gray level, as shown in Figure 8. With the present results, it is concluded that $\epsilon_f = 10^{-2}$ is a reasonable choice. It is worth noting that both converged levels are very low, which validates the registration results and the quality of the camera.

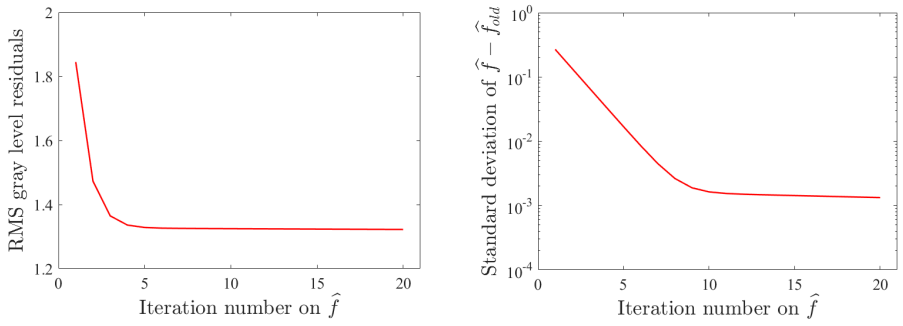

(a) (b)

Figure 8: (a) Change of root mean square gray level residuals and (b) the difference between two successive reference images $\widehat{f}(\boldsymbol{x})$ for the calibration phase

The difference between the first guess of the reference image and the converged $\widehat{f}(\boldsymbol{x})$, which is reported in Figure 9, shows a slight correction of $\widehat{f}(\boldsymbol{x})$ specific to the denoising procedure. The RMS difference between the initial estimate and the converged solution is equal to 1.29 gray level.

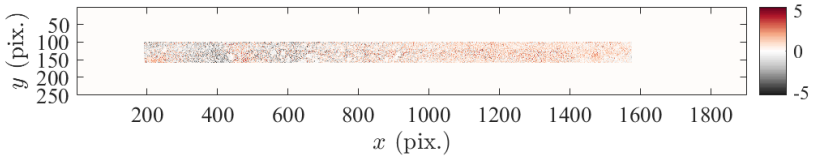

Figure 9: Difference between the denoised reference image and its initial estimate

The spacetime algorithm managed to capture the expected spatiotemporal displacements (Figure 10). In this figure, the spatial displacement and residual fields are shown for each beginning and end of all analyzed time increments. In the last subplot, the temporal information is highlighted with the red circle. The horizontal and vertical displacement fluctuations remain very small (*i.e.*, mostly of the order of 0.01 pixel or less for the whole step). Similarly, the gray level residuals reach very low values, as expected from the results of Figure 8(a). The overall gray level residuals are low (Figure 8(a)), which indicates that the spacetime procedure ran properly. Only a particular zone on the bottom left of the sample shows higher residuals (Figure 10).

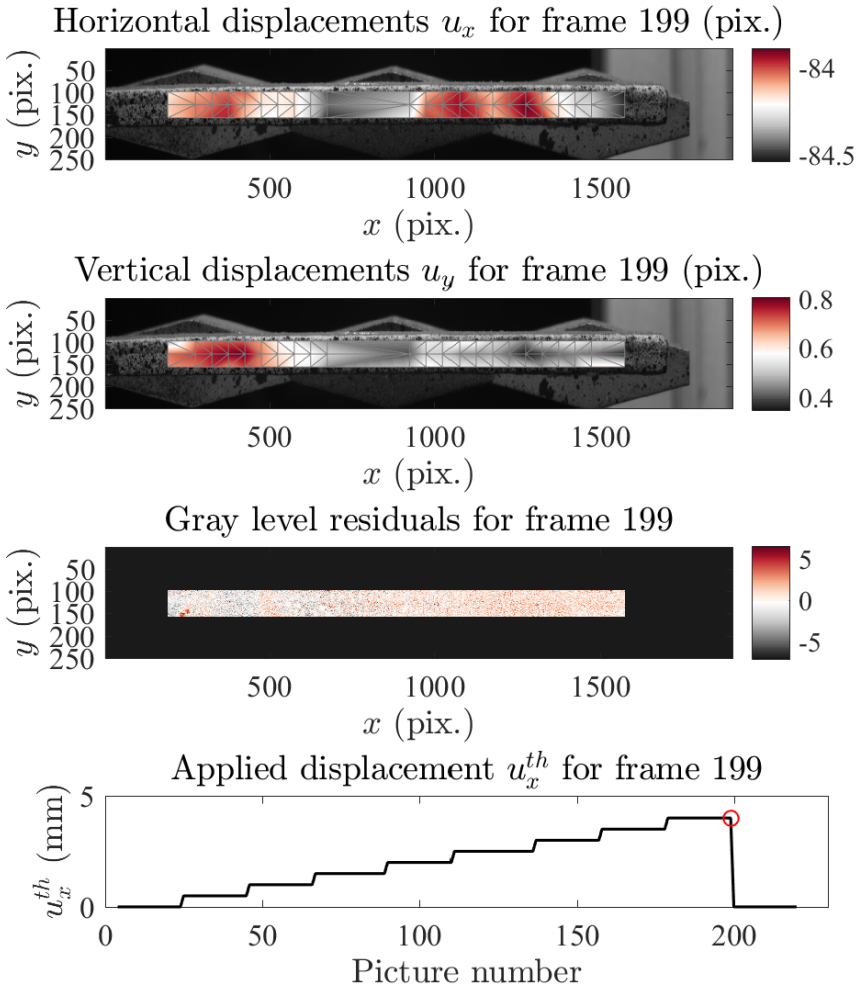

Figure 10: 2D displacements (expressed in pixels) and associated gray level residuals for picture № 199 (see red circle). Online version: corresponding movie for the 10 increments

For further analysis, a snapshot for a line of pixels containing that feature is shown in Figure 11. These residuals highlight the persistence of higher

levels of that particular pixel location (red area in the left part of some of the residual maps of Figure 10) that moves during calibration with an amplitude corresponding to the level of instantaneous horizontal displacements (*i.e.*, $\approx$ 10.5 pixels). Moreover, it is noted that the residual levels are slightly higher for the two time increments referring to the 0 mm position. Since it is a global spacetime procedure, the weight of these two increments is mitigated and the global residual level reduced, which emphasizes the interest of denoising the reference image by considering *all* images of the calibration phase.

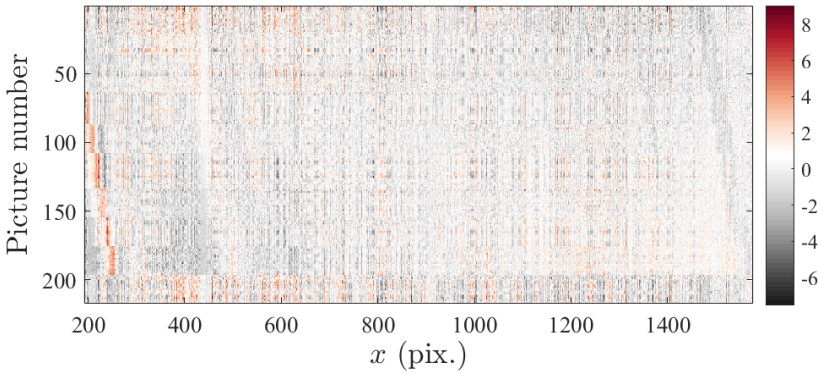

Figure 11: Spatiotemporal map of gray level residuals for a horizontal line of pixels (x from 192 to 1577 pixels) for $y = 141$ pixels

Figure 12 confirms that spacetime DIC reduces the overall residuals, in fact even better than instantaneous DIC even though the total number of kinematic degrees of freedom is ten times higher for the latter in comparison with the former. The reason for such a gain is associated with the denoising procedure that reduces the RMS residuals by $1 - 1/\sqrt{2} \approx 28$ %. In the present case, the mean reduction is equal to 26 %, which is very close to the

a priori estimate. When related to the initial gray level residuals (*i.e.*, with no displacement correction), there is a huge decrease that could be achieved thanks to the initialization procedure explained above. All these observations totally validate the present spacetime implementation based on Equation (2).

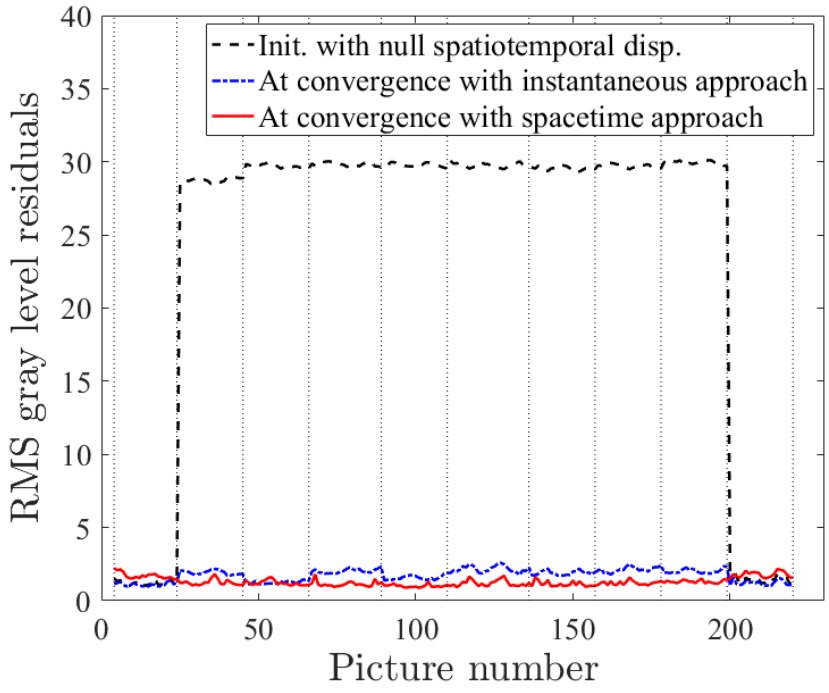

Figure 12: Root mean square gray level residuals for all analyzed pictures for instantaneous DIC (blue line), spacetime DIC (red line). The black line corresponds to the RMS gray level residuals of the raw picture difference (*i.e.*, with null displacements). The dotted vertical lines depict the time increments.

A byproduct of the calibration step is an accurate estimation of the physical pixel size. As a first approximation, it is calculated from the measured horizontal displacement u_x (expressed in pixels) compared with the

expected (metric) displacement u_x^{th} read on the micrometer screw. By using a least squares fit, the physical pixel size of one pixel is equal to 47.3 µm (or 21.1 pixel/mm). A more precise estimate is obtained by considering the L2-norm of displacements in order to account for misalignments between the picture frame and the actuator direction. The least squares fit (Figure 13) uses an affine function of slope 21.04 pixel/mm and an intercept of 2×10^{-2} pixel. Thus, the pixels have a physical size of 46.6 µm.

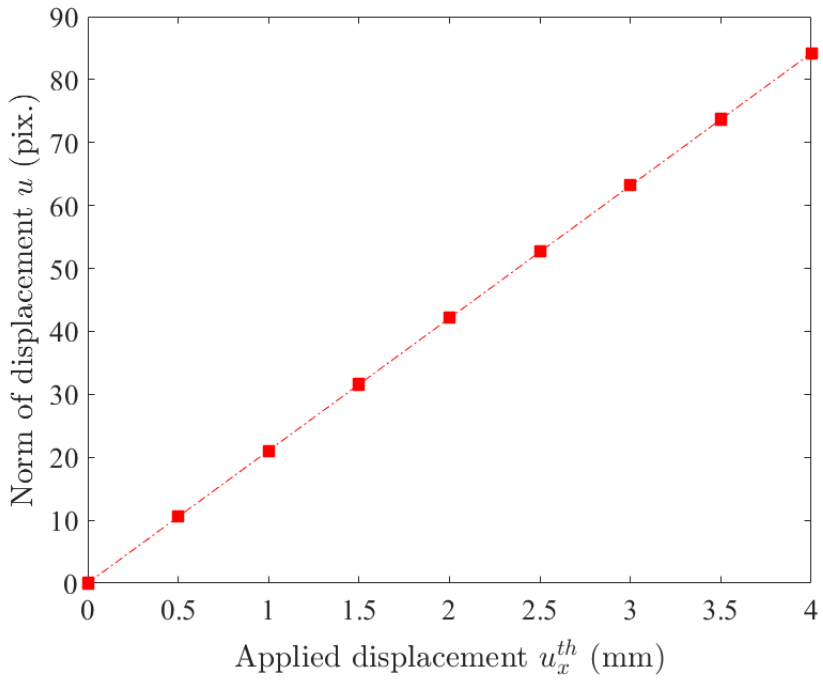

Figure 13: L2-norm of of measured displacements $\boldsymbol{u}_m(\boldsymbol{x}, t)$ vs. applied displacement

Figure 14 shows the standard deviations obtained for the horizontal and vertical displacements for both instantaneous and spatiotemporal approaches.

Each symbol corresponds to the average of all standard deviations calculated for each nodal displacement $u_x^i(t \in [t_{0,inc} : t_{f,inc}])$ and $u_y^i(t \in [t_{0,inc} : t_{f,inc}]))$ in the considered time increment inc, which is defined for t ranging from $t_{b,inc}$ and $t_{e,inc}$. The temporal regularization provided by the present approach allows the uncertainty levels to be decreased by a factor 4.9 (from 0.04 pixel to 0.008 pixel) for the horizontal displacements, and 5.8 for the vertical displacements (from 0.04 pixel to 0.007 pixel). This significant reduction illustrates the gain to be expected from spacetime analyses in which a denoised picture is computed.

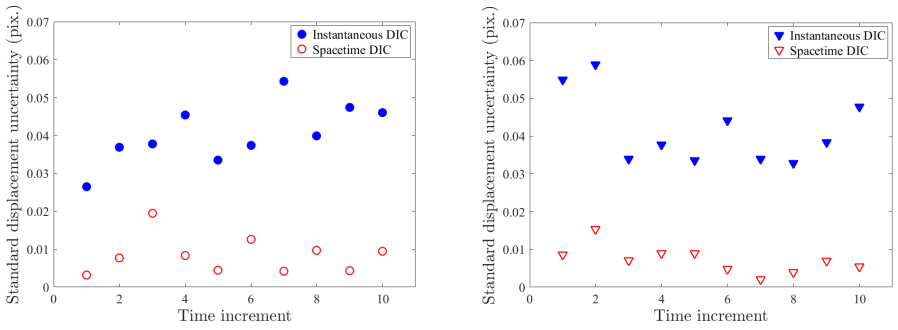

(a) (b)

Figure 14: Standard deviations on (a) horizontal and (b) vertical displacements for instantaneous and spacetime DIC procedures for the calibration phase

It is worth noting that the standard uncertainties reported for instantaneous DIC are higher than the usually expected levels (*i.e.,* of the order of 0.01 pixel for the chosen element size [28]). This could be the sign of a temporal modulation due to a heat haze effect at room temperature, and some gray level variations.

3.4. Heat haze analysis

The results for the second and third test steps (*i.e.,* heating/cooling without fan, and heating with fan) are now discussed. The instantaneous and spacetime DIC procedures are run on each step individually.

3.4.1. Instantaneous approach

Instantaneous DIC without using a specific treatment of the saturated areas (Figure 3) is first run, using as reference image $\widehat{f}_0(\boldsymbol{x})$ the mean of the 21 first images of the calibration phase (0 mm position). The mesh introduced in Section 3.2.1 is used hereafter to measure displacement fields. In the following analyses, specific nodes (Figure 15) will be highlighted:

1. Two nodes on both end sections of the mesh, in the centerline (node E in dark blue for the edge close to the clamp and node F in red for the free edge);
2. Two nodes close to the saturated area (Figure 3) in the middle of the sample (node C in cyan and node D in yellow);
3. A node affected by a surface defect (bulge) at the free edge of the sample (node G in purple).

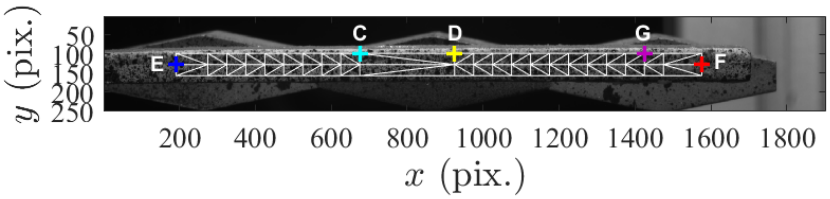

Figure 15: Initial reference image $\widehat{f}_0(\boldsymbol{x})$ with the meshed region of interest, and specific nodes, depicted by crosses, whose displacements are highlighted in Figure 16.

The instantaneous spatial displacement field $\boldsymbol{u}(\boldsymbol{x}, t)$ is initialized as $\mathbf{0}$. Because of gray level saturation, instantaneous DIC does not converge with the chosen criterion for pictures when the applied temperature is equal to $0.7T_{max}$ and T_{max}. Noisy results are observed in Figure 16 showing the displacements of all nodes. The displacements of the specific nodes introduced with their color code in Figure 15 are highlighted with thick crosses. Because of numerous saturated pixels (Figure 3), the gray level residuals will not decrease for the pixels located in that area. Since the instantaneous routine is global in space, displacements for nodes outside the saturated zone can still be used provided the corresponding gray levels residuals are checked. Some spikes of different origins are observed. Two major spikes appear in the analysis of the image series taken during the heating without fan (Figure 16(a-b) for pictures № 1950 and 3300) along with several minor spikes of lower amplitudes. Another major spike is highlighted in Figure 16(c-d) (for picture № 5050, during heating with fan). The major spikes are characterized by a global motion of all nodes (due to unexpected camera support motions) whereas the minor spikes are only due to spurious displacements of specific nodes affected by the saturated area.

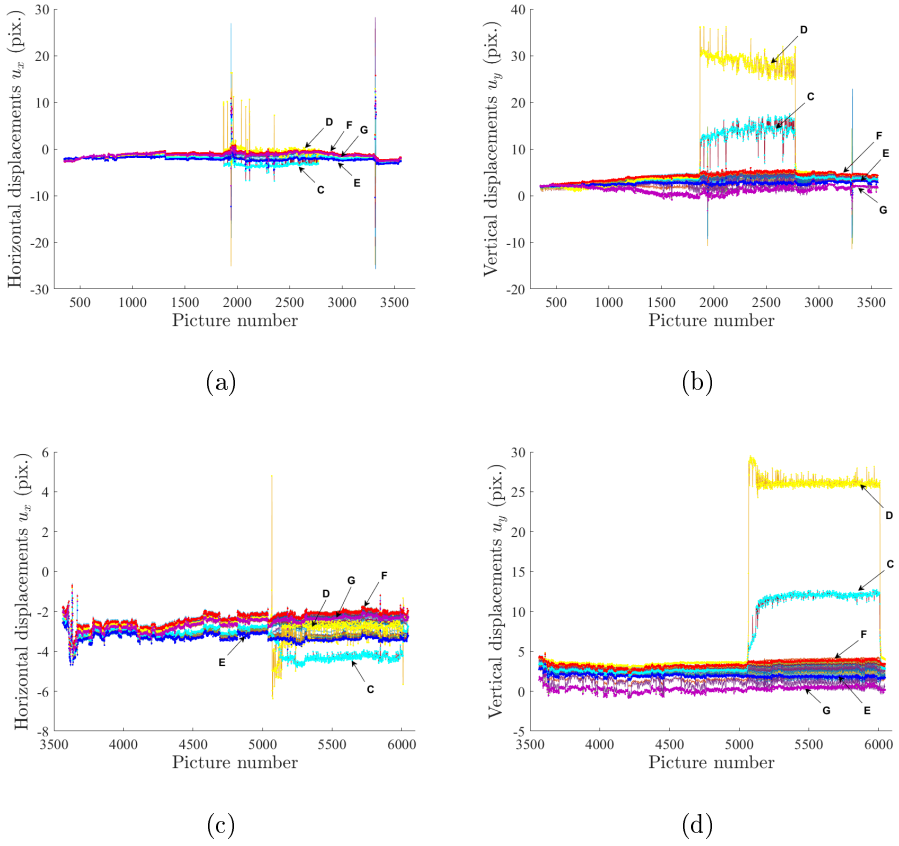

Figure 16: Nodal (a) horizontal u_x and (b) vertical u_y displacements (expressed in pixels) measured with instantaneous DIC for unmasked pictures from the heating phase with no fan. Nodal (c) horizontal u_x and (d) vertical u_y displacements (expressed in pixels) measured with instantaneous DIC for unmasked pictures from the heating phase with fan. The displacements plotted with thick crosses correspond to the five nodes (labeled as C, D, E, F and G) shown in Figure 15.

To overcome this issue, a mask is used to remove the saturated pixels (Figure 17). This operation is also performed on the denoised image, which means that these pixels are totally discarded from the DIC analyses, be they

instantaneous or spatiotemporal.

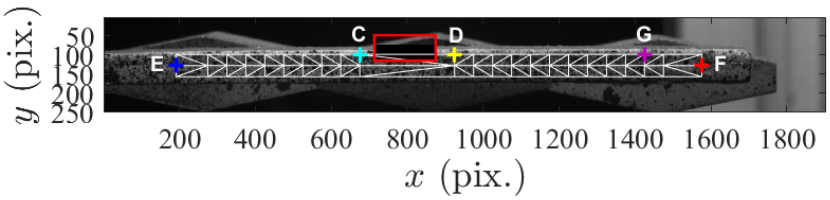

Figure 17: Reference image $\widehat{f}$ with the meshed region of interest, the masked zone (red box) and specific nodes, depicted with crosses, whose displacements are highlighted in Figures 18 and 19.

Even with the application of a mask, the instantaneous procedure does not converge for the pictures corresponding to $T = T_{max}$ for both heating phases and leads once again to unexpected global motions (Figure 18). To further address this issue, the mask could be made bigger, or this zone could be totally discarded and two smaller ROIs could be considered. This route was not followed since it will be shown that time regularization will provide sufficient robustness to fix this problem with the mask shown in Figure 17. However, it is interesting to notice that the minor spikes observed in Figure 16 are no longer present, thereby confirming their relation to saturated pixels. The biggest spikes remain, implying global displacements of the ROI (*i.e.*, camera support motion).

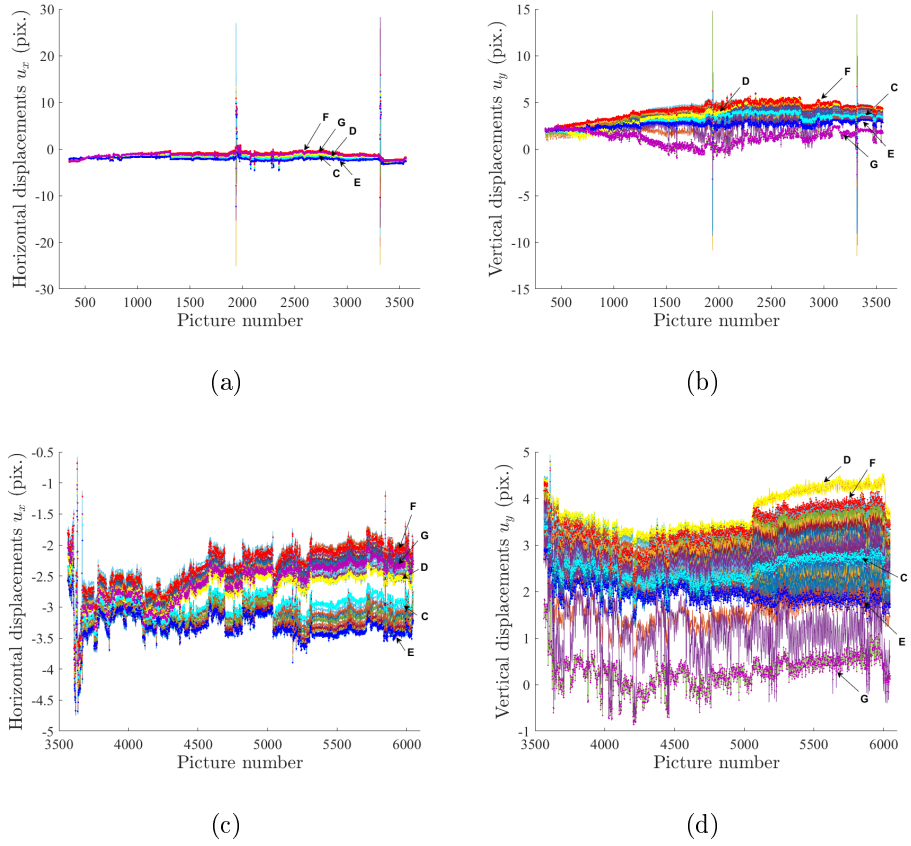

Figure 18: Nodal (a) horizontal u_x and (b) vertical u_y displacements measured with instantaneous DIC for masked pictures (heating without fan phase). Nodal (c) horizontal u_x and (d) vertical u_y displacements for masked pictures (heating with fan phase). The thick crosses correspond to the displacements of the five nodes shown in Figure 17.

The following analysis is now restricted to the displacements measured for the first and second temperature levels in Figure 19. Two observations can be made:

1. The heating phases lead to horizontal deformation of the sample of amplitude ca. 1.5 pixel corresponding to about 75 µm, and deflection

of ca. 1 pixel (or about 50 µm).

2. A temporal modulation is observed for the displacements that can be attributed to heat haze. The increase of fluctuations regarding displacements measured in the calibration step (*i.e.,* 0.04 pixel) and measured for the first temperature level (0.25 pixel for the transient state) support this assumption. Moreover, between the first and the second temperature levels, the fluctuations of nodal displacements increase, which can also be a sign of heat haze.

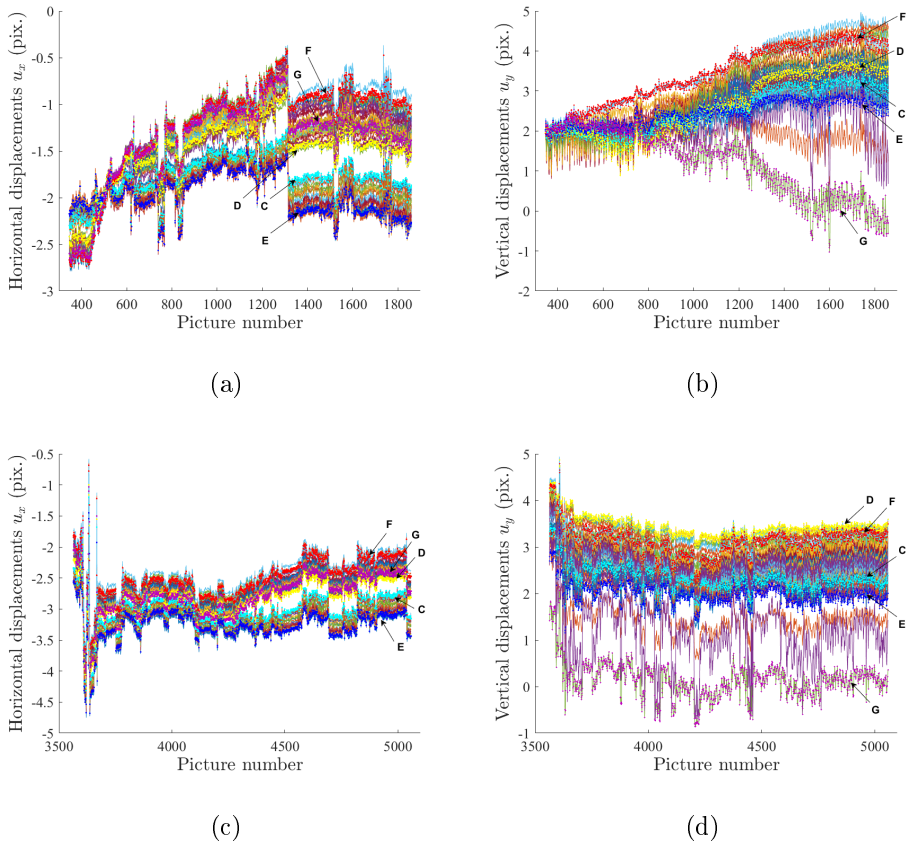

Figure 19: Nodal (a) horizontal u_x and (b) vertical u_y displacements measured with instantaneous DIC for masked pictures of first and second temperature levels (heating without fan phase). Nodal (c) horizontal u_x and (d) vertical u_y displacements measured with instantaneous DIC for masked pictures of first and second temperature levels (heating with fan phase). The thick crosses correspond to the displacements of the five nodes (labeled as C, D, E, F and G) introduced in Figure 17.

To assess the assumption of heat haze effect, a node is chosen from the left part of the CMC beam (*i.e.*, node R on the centerline of the sample and at a horizontal position of approximatively 375 pixels) as a reference.

The reference is chosen so that it is expected to be the least affected by the heat haze than the 11 selected nodes from the heated side and far from the laser beam. The nodal displacements of those nodes belonging to the right part of the beam (at the centerline of the sample for horizontal positions from 1025 pixels to 1575 pixels) are plotted as functions of that reference. The results for horizontal displacements (resp., vertical displacements) are shown for the heating phase with no fan in Figure 20(a) (resp., Figure 20(b)) and for the heating phase with fan in Figure 20(c) (resp., Figure 20(d)). Figure 20(e) shows the position of the reference node R (brown asterisk) and the 11 selected nodes in squares. The reported displacements are restricted to the second and third temperature levels where the heat haze effect is the more detectable. For the sake of legibility, the results obtained for the pictures responsible for the spikes in Figure 16 have been removed.

It is first observed that the nodes have relative displacements not only due to global motions representative of heating, which would essentially have given linear responses, but also by an additional effect. When comparing the relative displacements without and with fan, it appears that the fan reduces the amplitudes of the cloud, hence reduces the temporal variability. This property indicates that the heat haze affecting the displacements measurement at high temperatures is reduced when turning the fan on. On a more quantitative level, the fluctuations of the horizontal displacement are reduced from 1.05 pixel with no fan to 0.73 pixel when the fan is on for the horizontal component, and from 1.94 pixel to 1.75 pixel when the fan is on for the vertical component.

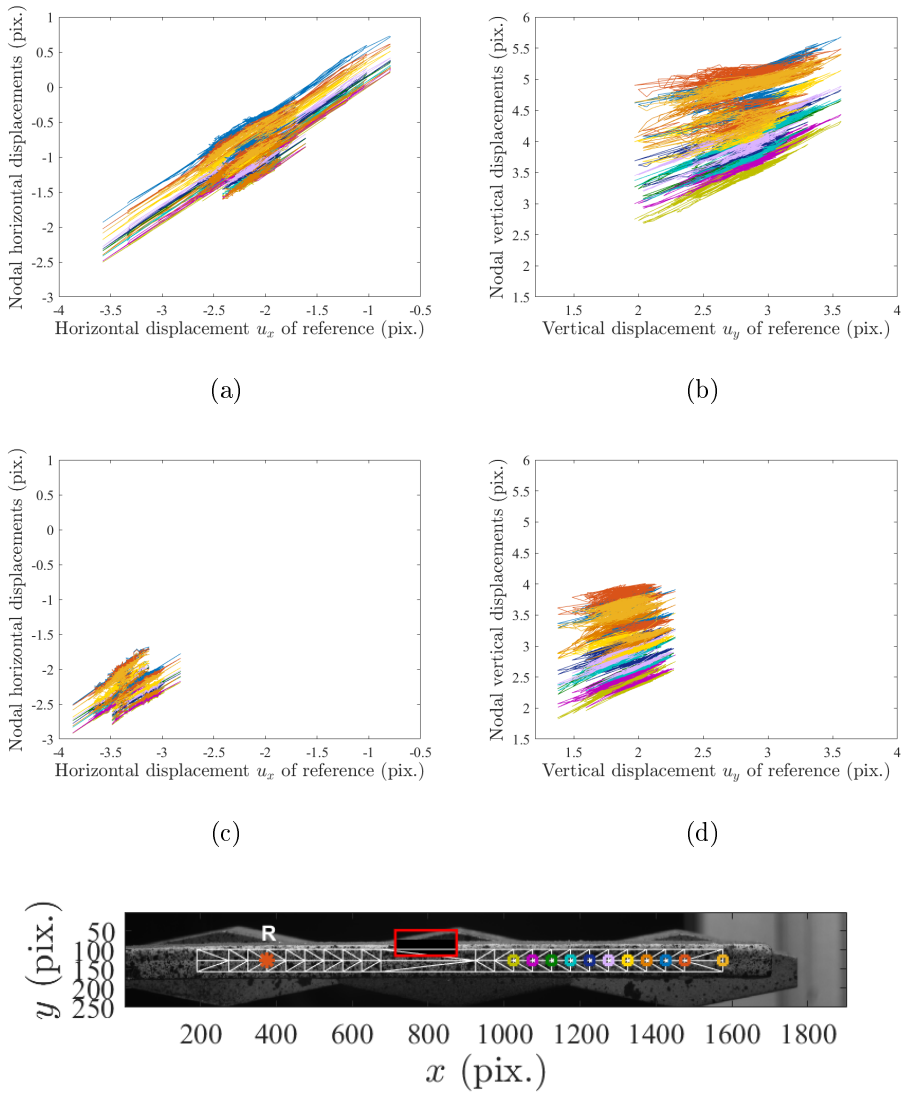

Figure 20: Nodal (a) horizontal u_x and (b) vertical u_y displacements (expressed in pixels) compared to a reference nodal displacement for the second and third temperature levels of the heating phase with no fan. Nodal (c) horizontal u_x and (d) vertical u_y displacements (expressed in pixels) compared to a reference nodal displacement for the second and third temperature levels of the heating phase with fan. (e) Locations of studied nodes in the mesh. Reference node R is depicted with an asterisk.

All these observations point to heat haze effects. The effect of temporal regularization on these effects is discussed in the sequel.

3.4.2. Temporal regularization

The last two test steps are analyzed by considering spacetime-DIC with the denoised reference image $\widehat{f}(\boldsymbol{x})$ constructed thanks to the calibration step and two picture series (with 3,218 and 2,485 images respectively). As previously, the mesh used to evaluate the nodal displacements is that introduced in Section 3.2.1 and the images are masked in the area corresponding to the saturated zone (Figure 17). The temporal shape functions are chosen linear and continuous between the time increments (Figure 21). The images corresponding to the second step (with no fan) are distributed in 10 time increments. For the third step, 9 time increments are considered.

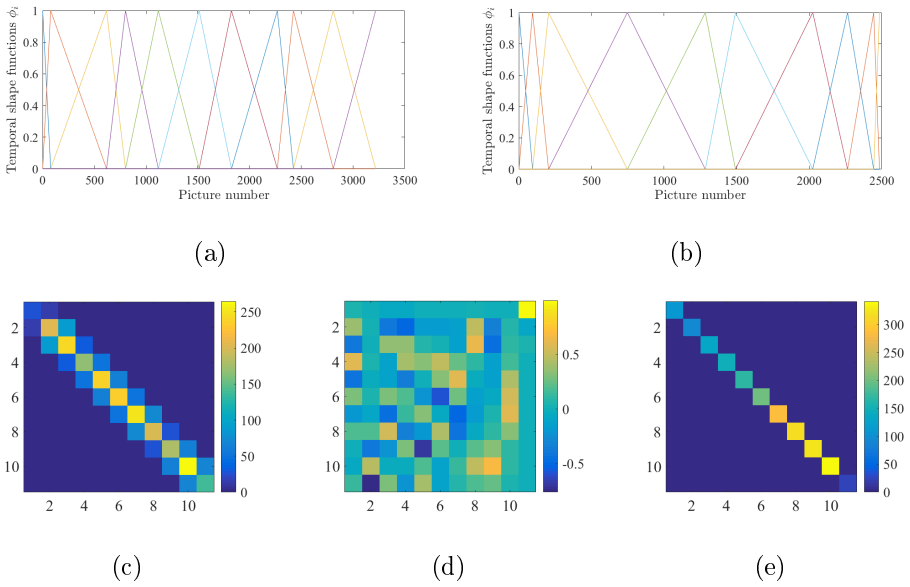

Figure 21: Temporal shape functions for the second (a) and third (b) steps of the experiment. (c) Global temporal operator [$\boldsymbol{\Phi}$], (d) eigen vector matrix [$\boldsymbol{V}$], and (e) diagonal matrix [$\boldsymbol{D}$] for the second step.

The global temporal operator [$\boldsymbol{\Phi}$], diagonal matrix [$\boldsymbol{D}$] and eigenvector matrix [$\boldsymbol{V}$] for the temporal shape functions of the second test step (Figure 21(a)) are shown in Figures 21(c-e). Because the length of the time increments is not uniform (*e.g.,* the first time increment in the second step contains 78 frames, whereas the next one includes 541 pictures), the eigen values of the diagonal matrix [$\boldsymbol{D}$] are more distributed than previously and vary between 241 and 25. However, the conditioning of the matrix is still very good (*i.e.,* 13 instead of 3 in the calibration step). Regarding the associated eigen vectors [$\boldsymbol{V}$], the continuity of the temporal shape functions and their non-orthogonality induces a more complex matrix than that obtained

in the calibration phase. Here, each temporal shape function contributes to modal shape functions.

The spatiotemporal nodal displacements $[\boldsymbol{a}_0]$ are initialized to $[\mathbf{0}]$. The algorithm converges in 14,300 s (*i.e.,* ca. 4 h) for the second test step, and 7,100 s (*i.e.,* ca. 2 h) for the third step, corresponding to a treatment of 4.4 frames/s for the first step and 2.9 frames/s. In comparison, the instantaneous procedure ran in 27,500 s (*i.e.,* 7 h and 40 min) for the second test step and in 16,000 s (*i.e.,* 4 h and 30 min) for the third step (corresponding to a treatment of 2.3 frame/s for the first step and 1.3 frame/s), which shows that spacetime approaches are faster than repeated instantaneous computations. Associated with the use of a coarse spatial mesh combined with the mask, spacetime DIC enables for a smoother and faster (*i.e.,* exponential) convergence (Figure 22) even with a severe criterion (*i.e.,* $\epsilon_a = 10^{-6}$).

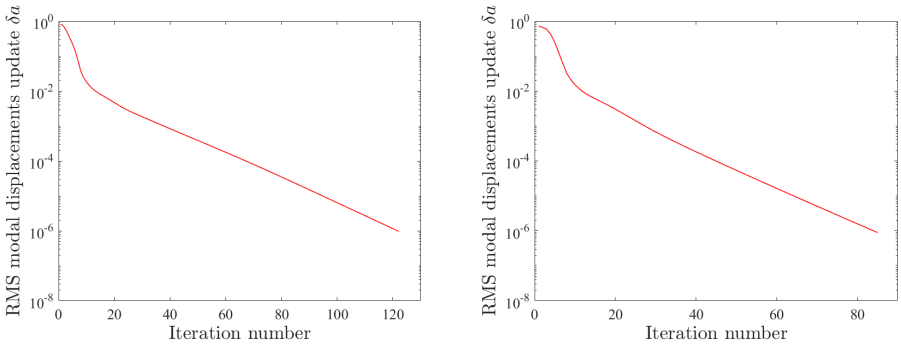

(a) (b)

Figure 22: Root mean square displacement difference $\boldsymbol{\delta a}$ for the second (a) and third (b) steps until $\|\boldsymbol{\delta a}\| < \epsilon_a$.

The change of gray level residuals is presented in Figure 23(a) for the

second step and Figure 23(b) for the third step. The overall residual levels are reduced at the end of the instantaneous and spacetime-DIC procedures. The residuals increase with the rise in temperature (and consequently saturation) even with the use of the mask. The gray level residuals of spacetime DIC are close to those of instantaneous DIC. The fluctuations of the former are more important than the latter, which is an indication that the two kinematic bases are different.

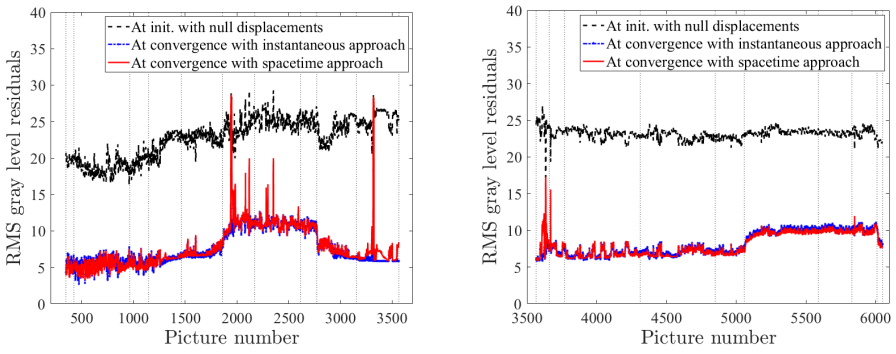

Figure 23: Root mean square gray level residuals for all analyzed pictures of the second (a) and third (b) steps when instantaneous (blue line) and spacetime (red line) DIC analyses are run. The black line corresponds to the RMS gray level residuals of the raw picture differences (*i.e.*, with null displacements). The dashed vertical lines depict the time increments.

Moreover, Figure 23(a) validates the fact that the lack of temporal shape functions adapted to the cooling path (that is the separation between transient and steady state parts) leads to higher levels for spacetime-DIC when compared to those obtained for the same temperature level for the heating

phase (from picture № 1148 to № 1860, which are divided into two time increments). For the first temperature level of the heating phase (steady state defined between pictures № 965 and № 1148), the mean gray level residual is equal to 5.3, whereas for the cooling path (steady state and transient defined as one interval for pictures from № 3155 to № 3565), the mean gray level residual reaches 7.2, that is 36 % higher.

Similarly, for the second temperature level of the heating phase (steady state defined between pictures № 1465 and № 1860), the mean gray level residual is equal to 7.1, whereas for the cooling path (for pictures from № 2771 to № 3155) it increases up to 7.4 (*i.e.,* 4 % increase). Hence a more adapted temporal mesh may help the overall residuals to be further reduced, especially in the cooling phase.

Last, in Figure 23(a), two peaks emerge in the spacetime-DIC residuals with their correspondence in the form of steps in the instantaneous-DIC residuals. They are related to an unexpected motion of the camera during the experiment that affects the corresponding images (Figure 16). The other spikes are also due spurious motions. For the instantaneous approach, this motion is well captured and has no consequence on the residual level, whereas the spatiotemporal approach forbids such sudden motions, and hence, only the residual shows a large increase at this instant. When such an artifact is detected and interpreted as irrelevant for the thermomechanical analysis, the concerned images can be disqualified, or a very local (in time) enrichment allowing for such sudden and large rigid body translation can be added. In the present case, these defective pictures are explained and are discarded. The new residuals obtained with this treatment are shown in Figure 24 and

the abnormal spikes have disappeared.

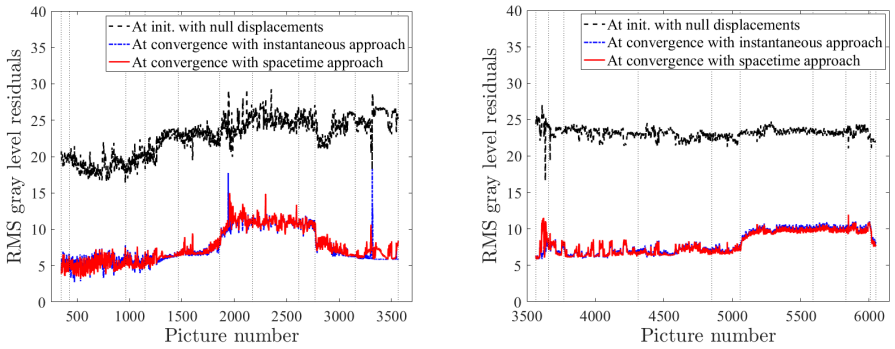

(a) (b)

Figure 24: Root mean square gray level residuals for all analyzed pictures of the second (a) and third (b) steps when instantaneous (blue line) and spacetime (red line) DIC analyses are run. For spacetime DIC, a temporal mask is used. The dashed line corresponds to the residuals of the raw picture differences (*i.e.,* with null displacements). The dotted vertical lines depict the time increments.

The converged spatiotemporal displacements are shown in Figure 25 for the second step and in Figure 26 for the third step. When analyzing the results for the steady states (heating path for the case with no fan), an increasing longitudinal expansion of the CMC beam is observed, with horizontal displacement amplitudes of 0.8 pixel (*i.e.,* $\approx$ 37.3 µm) for the first temperature level ($0.4T_{\max}$, frame № 1148), and 1.3 pixel (*i.e.,* $\approx$ 60.6 µm) for both second and third temperature levels corresponding respectively to $0.7T_{\max}$ (frame № 1860) and $T_{\max}$ (frame № 2771). A (downward) deflection of the sample with an inflexion point located at the center of the beam is also observed.

Regarding the results obtained for the last two time increments (defined between frames № 2771 and № 3155, and between frames № 3155 and № 3565), it is not possible to conclude on the displacement shape because the temporal basis appears poor and interpolates the sought displacements for a unique step containing transient/steady state phases.

Last, the mask managed to remove the biggest part of the saturation area, leading to consistent spatiotemporal displacements and lower residuals. However, as seen on the plots of vertical displacements u_y measured for the second and third temperature levels and on the residuals, the saturation effect is still identifiable as well as a bulge at the free edge of the beam ($x \approx$ 1500 pixels), corresponding to a surface flaw.

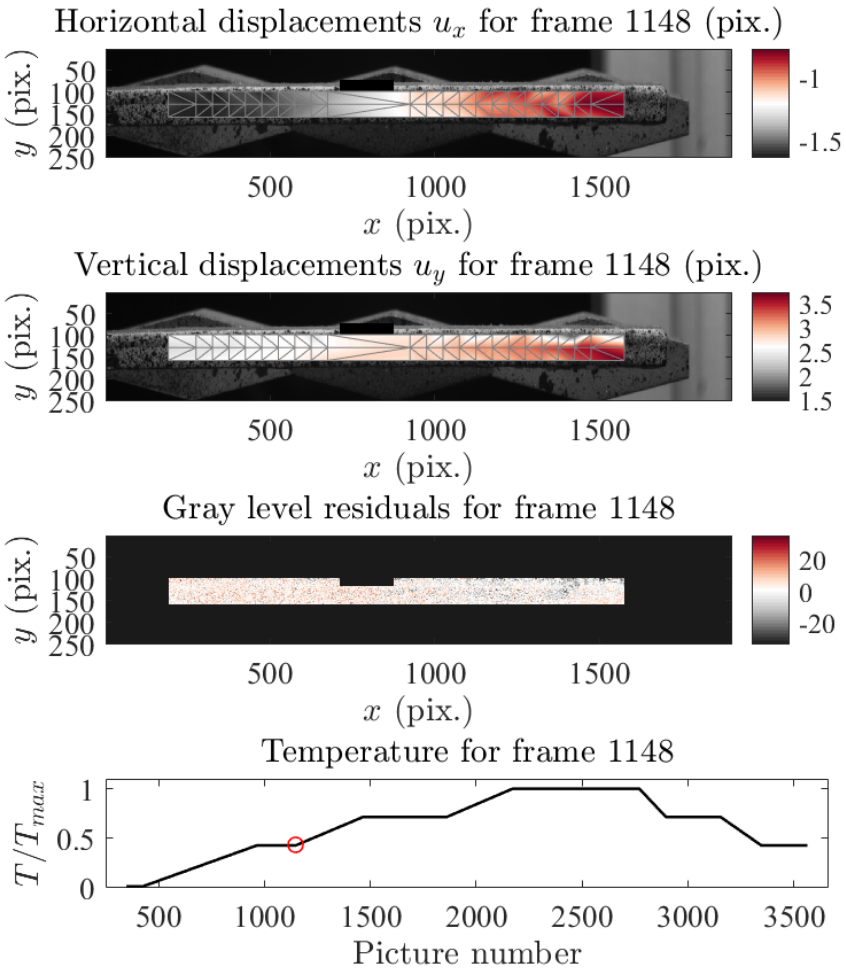

Figure 25: 2D displacements (expressed in pixels) and associated gray level residuals for picture № 1148 (see red circle). Online version: corresponding movie for the 11 increments

For the results of the heating phase with fan on, the results are similar to those presented above in terms of overall trends. In that case, the increase

of longitudinal expansion is more pronounced than previously since the horizontal displacement amplitude varies from 0.7 pixel (*i.e.,* $\approx$ 32.6 µm) for the first temperature level to 1.3 pixel (*i.e.,* $\approx$ 60.6 µm) for the third temperature level, with an intermediate value of 1.1 pixel (*i.e.,* $\approx$ 51.3 µm) for the second temperature level. This is a first indication that the addition of a fan improves the quality of the results, making their interpretation easier.

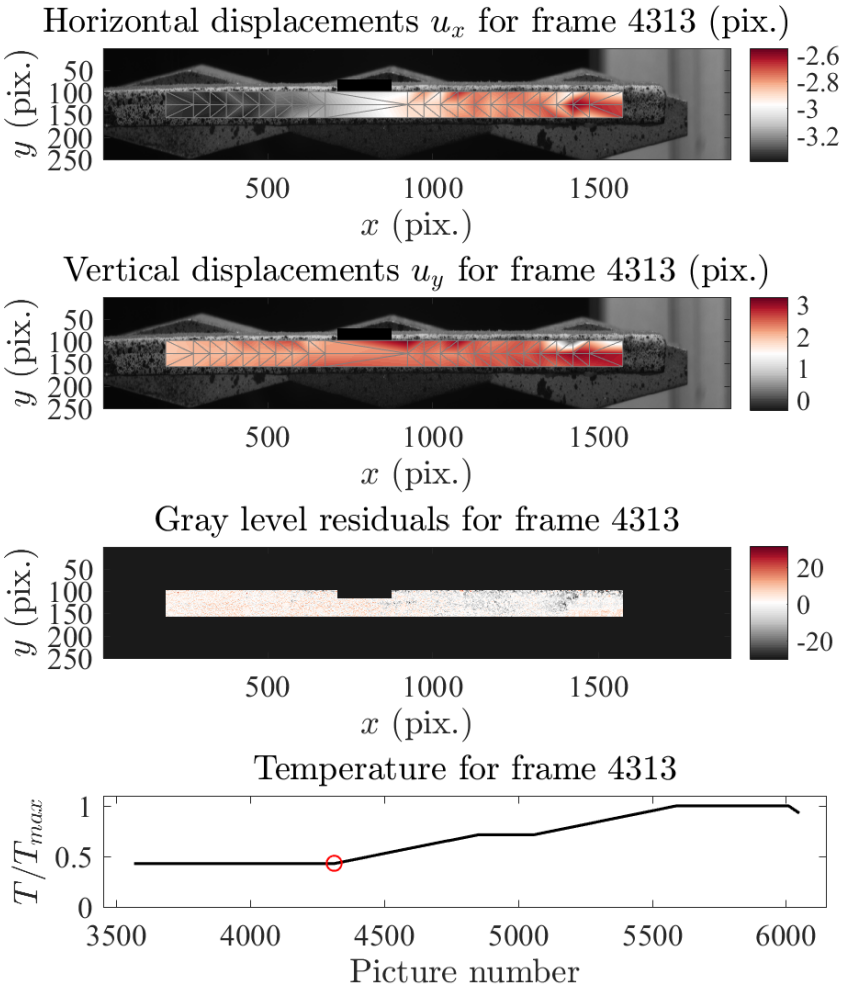

Figure 26: 2D displacements (expressed in pixels) and associated gray level residuals for picture № 4313 (see red circle). Online version: corresponding movie for the 10 increments

By only analyzing the 2D displacements, and especially by comparing the displacements between the first and second time increments of the heating

phase with fan (defined respectively in Figure 26 between frames № 3566 and № 3660, and between frames № 3660 and № 3770), it is not easy to conclude on the utility of the fan. To assess its influence on the heat haze effect (*i.e.,* temporal variations), the change of the standard deviation of measured nodal displacements calculated for each time increment is shown in Figure 27. The reported values correspond to the mean over all nodes of the temporal standard deviation for nodal displacements. The first ten time increments refer to the calibration phase, the time increments from 11 to 20 are related to second step (*i.e.,* heating/cooling with no fan), and the last nine time increments are associated with the third step (*i.e.,* heating with fan on). The fan is turned on at the beginning of time increment № 22.

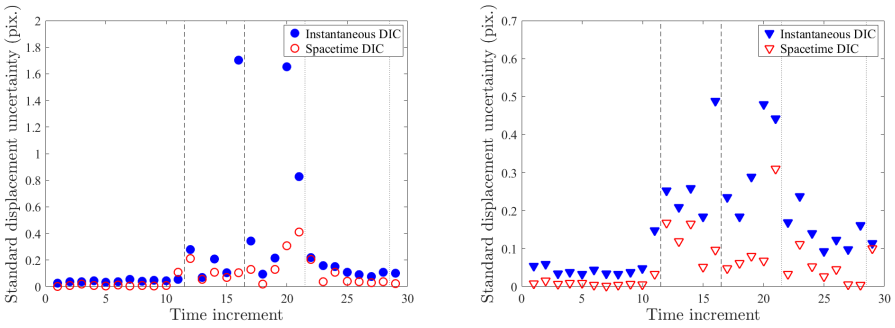

(a) u_x (b) u_y

Figure 27: Standard deviations of (a) horizontal and (b) vertical nodal displacements for instantaneous and spacetime DIC for the whole experiment. The vertical dashed lines correspond to the heating phase of the second step. The vertical dotted lines correspond to the heating phase of the third step.

First, it is worth noting that the spacetime approach has reduced the level of temporal variations of both vertical and horizontal displacements

compared to the instantaneous approach. As expected, spatiotemporal DIC filtered out a significant part of the temporal modulations due to the heat haze. Second, to compare the effect of the fan on the temporal fluctuations, only the values corresponding to heating phases calculated via spacetime-DIC are taken into account (*i.e.,* time increments № 12 to 16 for the heating step with no fan and time increments № 22 to 28 for the heating step with fan, see Figure 27). When restricted to the steady state levels of the heating phases (*i.e.,* time increments 13, 15, 17, 18 with no fan case, and 22, 23, 25, 27 when the fan is on), the mean horizontal fluctuations go from 0.07 pix to 0.08 pixel, and from 0.07 pixel to 0.04 pixel in the vertical direction. The latter is more critical for assessing the beam deflection (*i.e.,* a decrease of 40 %). The fan has a significant effect on the temporal fluctuations in the direction perpendicular to the created air flow.

4. Conclusion

A new implementation of global spacetime DIC was proposed herein. It is based on a modal decomposition of the measured displacement field. This approach allows standard (*i.e.,* instantaneous) DIC codes to be extended to spacetime analyses with minimal changes. Such strategies can be extended to stereocorrelation and even digital volume correlation. As shown herein, such approaches allow the measurement uncertainties to be decreased. In the present experimental configuration in which brightness conservation was not satisfied and gray level saturation occurred, it was shown that global (in time) analyses provide sufficient regularization. Without the latter, instantaneous analyses could not converge.

The second novelty of this paper is associated with the construction of a denoised reference picture by considering a whole set of images (*i.e.,* 217 pictures in the present case). This is an important step associated with spacetime analyses for which the reference picture plays an important role in comparison with all the other pictures. With the present procedure, it was shown that the measurement uncertainties could be drastically reduced.

The experimental test that was studied herein led to very high temperatures on the sample surface (*i.e.,* greater than 1,200°C in the heat affected zone by the laser beam). Since no special heat insulation was required, heat haze effects occurred, which induced rather high displacement fluctuations in comparison with the longitudinal and transverse deformations of the SiC/SiC composite. It was shown that the use of a small fan could reduce by half the displacement fluctuations, which is in agreement with earlier observations [12]. Such studies may also be carried out at room temperature to check such biasing effects.

With the present results, the longitudinal elongations induced by the heterogeneous temperature field could be properly captured. Conversely, the deflection of the sample remains more difficult to quantify. Additional regularizations based, for instance, on beam kinematics [39], or equilibrium gap [40] may allow the vertical deflection to be better assessed. Such information will be complemented by the analyses of the stereovision system data [41], and the thermal measurements that could be associated through hybrid multi-view correlation [35, 42]. The 3D displacement fields of the sample front face will also be regularized with the same strategy as presented herein in order to obtain measurements with lower uncertainties and fluctuations, which will

be used for the calibration of the thermomechanical properties of the studied composite.

Acknowledgments

This work was supported under PRC MECACOMP, French research project co-funded by DGAC and SAFRAN Group, managed by SAFRAN Group and involving SAFRAN Group, ONERA and CNRS.

References

[1] Advisory Council for Aviation Research and Innovation in Europe, Strategic Research & Innovation Agenda, http://www.acare4europe.org, 2017.

[2] N. Bansal, Handbook of Ceramic Composites, Springer US, 2005.

[3] F. Zok, Ceramic-matrix composites enable revolutionary gains in turbine engine efficiency 95 (2016) 22–28.

[4] M. Appleby, D. Zhu, G. Morscher, Mechanical properties and real-time damage evaluations of environmental barrier coated SiC/SiC CMCs subjected to tensile loading under thermal gradients, Surf. Coat. Technol. 284 (2015) 318–326.

[5] A. Burr, F. Hild, F. Leckie, Behaviour of ceramic-matrix composites under thermomechanical cyclic loading conditions, Compos. Sci. Tech. 58 (5) (1998) 779–783.

[6] J. Brennan, Interfacial characterization of a slurry-cast melt-infiltrated SiC/SiC ceramic-matrix composite, Acta Mat. 48 (18) (2000) 4619–4628.

[7] A. Burr, F. Hild, F. Leckie, Isochronous analysis of ceramic-matrix composites under thermomechanical cyclic loading conditions, Compos. Sci. Tech. 61 (15) (2001) 2231–2238.

[8] G. Morscher, Tensile creep and rupture of 2D-woven SiC/SiC composites for high temperature applications, J. Europ. Ceram. Soc. 30 (11) (2010) 2209–2221.

[9] Y. Gowayed, G. Ojard, J. Chen, G. Morscher, R. Miller, U. Santhosh, J. Ahmad, R. John, Accumulation of time-dependent strain during dwell-fatigue experiments of iBN-Sylramic melt infiltrated SiC/SiC composites with and without holes, Compos. Part A 42 (12) (2011) 2020–2027.

[10] M. Grédiac, F. Hild (Eds.), Full-Field Measurements and Identification in Solid Mechanics, ISTE / Wiley, London (UK), 2012.

[11] M. Sutton, J. Orteu, H. Schreier, Image correlation for shape, motion and deformation measurements: Basic Concepts, Theory and Applications, Springer, New York, NY (USA), 2009.

[12] J. Lyons, J. Liu, M. Sutton, High-temperature deformation measurements using digital-image correlation, Exp. Mech. 36 (1) (1996) 64–70.

[13] J. Liu, J. Lyons, M. Sutton, A. Reynolds, Experimental characterization of crack tip deformation fields in alloy 718 at high temperatures, ASME J. Eng. Mater. Technol. 120 (1) (1998) 71–78.

[14] B. Grant, H. Stone, P. Withers, M. Preuss, High-temperature strain field measurement using digital image correlation, J. Strain Analysis 44 (4) (2009) 263–271.

[15] B. Pan, D. Wu, Z. Wang, Y. Xia, High-temperature digital image correlation method for full-field deformation measurement at 1200 °c, Meas. Sci. Technol. 22 (1) (2011) 015701.

[16] J. Hammer, J. Seidt, A. Gilat, Strain Measurement at Temperatures Up to 800 °C Utilizing Digital Image Correlation, Springer International Publishing, 2014, pp. 167–170.

[17] M. Novak, F. Zok, High-temperature materials testing with full-field strain measurement: Experimental design and practice, Rev. Sci. Instrum. 82 (11) (2011) 115101.

[18] B. Pan, D. Wu, Y. Xia, High-temperature deformation field measurement by combining transient aerodynamic heating simulation system and reliability-guided digital image correlation, Opt. Lasers Eng. 48 (9) (2010) 841–848.

[19] P. Leplay, J. Réthoré, S. Meille, M.-C. Baietto, Damage law identification of a quasi brittle ceramic from a bending test using digital image correlation, J. Europ. Ceram. Soc. 30 (13) (2010) 2715–2725.

[20] P. Leplay, O. Lafforgue, F. Hild, Analysis of Asymmetrical Creep of a Ceramic at 1350°C by Digital Image Correlation, J. Am. Ceram. Soc. 98 (7) (2015) 2240–2247.

[21] M. Sutton, Computer vision-based, noncontacting deformation measurements in mechanics: A generational transformation, Appl. Mech. Rev. 65 (AMR-13-1009) (2013) 050802.

[22] M. De Strycker, L. Schueremans, W. Van Paepegem, D. Debruyne, Measuring the thermal expansion coefficient of tubular steel specimens with digital image correlation techniques, Opt. Lasers Eng. 48 (10) (2010) 978–986.

[23] A. Maynadier, M. Poncelet, K. Lavernhe-Taillard, S. Roux, One-shot measurement of thermal *and* kinematic fields: Infra-red image correlation (iric), Exp. Mech. 52 (3) (2011) 241–255.

[24] A. Charbal, J.-E. Dufour, A. Guery, F. Hild, S. Roux, L. Vincent, M. Poncelet, Integrated digital image correlation considering gray level and blur variations: Application to distortion measurements of ir camera, Opt. Lasers Eng. 78 (2016) 75–85.

[25] R. Berke, J. Lambros, Ultraviolet digital image correlation (UV-DIC) for high temperature applications, Rev. Sci. Instrum. 85 (4) (2014) 045121.

[26] F. Hild, S. Roux, Digital image correlation, in: P. Rastogi, E. Hack (Eds.), Optical Methods for Solid Mechanics. A Full-Field Approach, Wiley-VCH, Weinheim (Germany), 2012, pp. 183–228.

[27] B. Pommier, F. Hild, E. Charkaluk, Analyse d'une éprouvette de fatigue thermomécanique par corrélation d'images, in: Y. Berthaud, M. Cottron, J. Dupré, F. Morestin, J. Orteu, V. Valle (Eds.), Photomécanique 2001, GAMAC, 2001, pp. 359–366.

[28] F. Hild, S. Roux, Comparison of local and global approaches to digital image correlation, Exp. Mech. 52 (9) (2012) 1503–1519.

[29] G. Broggiato, L. Casarotto, Z. Del Prete, D. Maccarrone, Full-field strain rate measurement by white-light speckle image correlation, Strain 45 (4) (2009) 364–372.

[30] G. Besnard, S. Guérard, S. Roux, F. Hild, A space-time approach in digital image correlation: Movie-DIC, Optics Lasers Eng. 49 (2011) 71–81.

[31] G. Besnard, H. Leclerc, S. Roux, F. Hild, Analysis of image series through digital image correlation, J. Strain Analysis 47 (4) (2012) 214–228.

[32] J. Neggers, J. Hoefnagels, M. Geers, F. Hild, S. Roux, Time-resolved integrated digital image correlation, Int. J. Num. Meth. Eng. 203 (3) (2015) 157–182.

[33] A. Charbal, S. Roux, F. Hild, L. Vincent, Spatiotemporal regularization for digital image correlation: Application to infrared camera frames, Int. J. Num. Meth. Eng. (DOI: 10.1002/nme.5788).

[34] M. Berny, C. Jailin, A. Bouterf, F. Hild, S. Roux, Model Reduction for Space-Time DIC, submitted for publication.

[35] J.-E. Dufour, F. Hild, S. Roux, Shape, Displacement and Mechanical Properties from Isogeometric Multiview Stereocorrelation, J. Strain Analysis 50 (7) (2015) 470–487.

[36] H. Leclerc, J. Neggers, F. Mathieu, F. Hild, S. Roux, Correli 3.0, IDDN.FR.001.520008.000.S.P.2015.000.31500, Agence pour la Protection des Programmes, Paris (France) (2015).

[37] H. Leclerc, J. Périé, S. Roux, F. Hild, Integrated digital image correlation for the identification of mechanical properties, Vol. LNCS 5496, Springer, Berlin (Germany), 2009, pp. 161–171.

[38] D. Demange, P. Beauchêne, M. Bejet, R. Casulleras, Mesure simultanée de la diffusivité thermique selon les deux directions principales d'un matériau, Revue Générale de Thermique 36 (10) (1997) 755–770.

[39] F. Hild, S. Roux, R. Gras, N. Guerrero, M. Marante, J. Flórez-López, Displacement measurement technique for beam kinematics, Optics Lasers Eng. 47 (2009) 495–503.

[40] Z. Tomičević, F. Hild, S. Roux, Mechanics-aided digital image correlation, J. Strain Analysis 48 (2013) 330–343.

[41] J.-E. Dufour, B. Beaubier, F. Hild, S. Roux, CAD-based displacement measurements. Principle and first validations, Exp. Mech. 55 (9) (2015) 1657–1668.

[42] A. Charbal, J.-E. Dufour, F. Hild, M. Poncelet, L. Vincent, S. Roux, Hybrid stereocorrelation using infrared and visible light cameras, Exp. Mech. 56 (2016) 845–860.